

# UCLA

## UCLA Previously Published Works

### Title

Calibration and Limitations of the Mg ii Line-based Black Hole Masses

### Permalink

<https://escholarship.org/uc/item/8zz8r6gk>

### Journal

The Astrophysical Journal, 859(2)

### ISSN

0004-637X

### Authors

Woo, Jong-Hak  
Le, Huynh Anh N  
Karouzos, Marios  
et al.

### Publication Date

2018-06-01

### DOI

10.3847/1538-4357/aabf3e

Peer reviewed

## CALIBRATION AND LIMITATIONS OF THE MG II LINE-BASED BLACK HOLE MASSES

JONG-HAK WOO<sup>1</sup>, HUYNH ANH N. LE<sup>1</sup>, MARIOS KAROUZOS<sup>1</sup>, DAWOO PARK<sup>1</sup>, DAESEONG PARK<sup>2</sup>, MATTHEW A. MALKAN<sup>3</sup>,  
TOMMASO TREU<sup>3</sup>, AND VARDHA N. BENNETT<sup>4</sup>

<sup>1</sup>Astronomy Program, Department of Physics and Astronomy, Seoul National University, Seoul, 151-742, Republic of Korea

<sup>3</sup>Korea Astronomy and Space science Institute, Daejeon, Republic of Korea

<sup>4</sup>Physics Department, California Polytechnic State University, San Luis Obispo, CA 93407, USA

*Draft Version,*

### ABSTRACT

We present the single-epoch black hole mass ( $M_{\text{BH}}$ ) calibrations based on the rest-frame UV and optical measurements of Mg II 2798Å and H $\beta$  4861Å lines and AGN continuum, using a sample of 52 moderate-luminosity AGNs at  $z \sim 0.4$  and  $z \sim 0.6$  with high-quality Keck spectra. We combine this sample with a large number of luminous AGNs from the Sloan Digital Sky Survey to increase the dynamic range for a better comparison of UV and optical velocity and luminosity measurements. With respect to the reference  $M_{\text{BH}}$  based on the line dispersion of H $\beta$  and continuum luminosity at 5100Å, we calibrate the UV and optical mass estimators, by determining the best-fit values of the coefficients in the mass equation. By investigating whether the UV estimators show systematic trend with Eddington ratio, FWHM of H $\beta$ , the Fe II strength, and the UV/optical slope, we find no significant bias except for the slope. By fitting the systematic difference of Mg II-based and H $\beta$ -based masses with the  $L_{3000}/L_{5100}$  ratio, we provide a correction term as a function of the spectral index as  $\Delta C = 0.24(1 + \alpha_\lambda) + 0.17$ , which can be added to the Mg II-based mass estimators if the spectral slope can be well determined. The derived UV mass estimators typically show  $> \sim 0.2$  dex intrinsic scatter with respect to H $\beta$ -based  $M_{\text{BH}}$ , suggesting that the UV-based mass has an additional uncertainty of  $\sim 0.2$  dex, even if high quality rest-frame UV spectra are available.

*Subject headings:* galaxies: active – galaxies: nuclei – galaxies: Seyfert

### 1. INTRODUCTION

One of the most fundamental properties of active galactic nuclei (AGNs) is black hole mass ( $M_{\text{BH}}$ ), which sets the upper limit of AGN energetics via the Eddington limit.  $M_{\text{BH}}$  also represents the integration of mass accretion over the life time of a given black hole (BH), connecting the growth histories of galaxies and BHs as implied by the observed correlation between  $M_{\text{BH}}$  and host galaxy properties (e.g., Kormendy & Ho 2013; Woo et al. 2013).

Estimating  $M_{\text{BH}}$  became a routine process for type 1 AGNs, which are characterized by the presence of broad emission lines, since various single-epoch mass estimators were developed based on the empirical results from reverberation-mapping studies. While the size of the broad-line region (BLR) is measured from the time lag between the light curves of AGN continuum and broad emission line flux in the reverberation-mapping studies (Blandford & McKee 1982; Peterson 1993), which requires a long-term monitoring campaign (e.g., Wandel et al. 1999; Kaspi et al. 2000; Peterson et al. 2004; Bentz et al. 2009; Barth et al. 2011; Grier et al. 2013; Barth et al. 2015; Fausnaugh 2017; Park et al. 2017), the single-epoch estimators utilize the empirical size-luminosity relation obtained from the reverberation studies. As a proxy for the BLR size, the monochromatic luminosity at 5100Å can be used to indirectly infer the BLR size based on the empirical relation (e.g., Kaspi et al. 2000, 2005; Bentz et al. 2006, 2013).

Since the size-luminosity relation provides a powerful simple method for determining  $M_{\text{BH}}$ , which only requires single spectroscopic observation, it has been applied to a large sample of type 1 AGNs (e.g., Woo & Urry 2002; McLure & Dunlop 2004; Shen et al. 2011). While the H $\beta$  line was

the main tool to measure the time lag in the reverberation-mapping studies, hence, the size-luminosity relation is best-calibrated with the H $\beta$  line, the single epoch method with various recipes became applicable to type 1 AGNs at higher redshift. In this case, the rest-frame UV continuum and emission lines obtained in large optical spectroscopic surveys, e.g., Sloan Digital Sky Survey (SDSS) are typically used to estimate  $M_{\text{BH}}$ . For example, a combination of the Mg II 2798Å line velocity and near-UV continuum luminosity has been used for AGNs at  $0.4 < z < 2$  (e.g., McLure & Dunlop 2004; Vestergaard & Peterson 2006; McGill et al. 2008; Wang et al. 2009; Shen et al. 2011), while the pair of the velocity of C IV 1549Å line and AGN continuum luminosity in the Far-UV is often adopted for AGNs at  $z > \sim 2$  (e.g., Shen et al. 2011; Karouzos et al. 2015).

By combining the virial assumption, i.e., the BLR gas is mainly governed by the gravitational potential of the central BH, and the size-luminosity relation between BLR size ( $R_{\text{BLR}}$ ) and continuum luminosity ( $L$ ) as  $R_{\text{BLR}} \propto L^{\sim 0.5}$ ,  $M_{\text{BH}}$  can be expressed as,

$$\log M_{\text{BH}} = \alpha + \beta \log V + \gamma \log L \quad (1)$$

where  $V$  is the velocity measured from the width of a broad emission line. For H $\beta$ -based mass estimators,  $\beta$  is fixed as 2, based on the virial theorem. However the value of  $\beta$  can differ from 2 as the comparison between H $\beta$  line width and the line width of other broad emission lines often shows a non-linear relationship (e.g., Wang et al. 2009; Marziani et al. 2013). In the case of  $\gamma$ , the most updated H $\beta$  size luminosity relation study reported  $\gamma = 0.533^{+0.035}_{-0.033}$  (Bentz et al. 2013), which is consistent with a naive photoionization assumption (Wandel et al. 1999), while for other luminosity measures, i.e., UV contin-

uum or line luminosities, the value can also vary.

The alternative UV mass estimators are calibrated compared to the  $H\beta$ -based mass estimators. Since the directly measured time-lag (i.e., BLR size) based on the variability of Mg II has been limited to only a small number of objects (Reichert et al. 1994; Metzroth et al. 2006; Shen et al. 2016), due to the observational difficulties and/or the lack of consistent variability between line and continuum (Woo 2008; Cackett et al. 2015), there is no available Mg II-based size-luminosity relation. Thus, UV mass estimators need to be calibrated with  $H\beta$ -based measurements, i.e., time lags and mass estimates. Using the reverberation-mapped AGN sample, for example, McLure & Jarvis (2002) compared the  $H\beta$ -based BLR size with the UV luminosity at 3000 Å ( $L_{3000}$ ), and provided a recipe of  $M_{BH}$  determination based on  $L_{3000}$  and the FWHM of Mg II, (see also McLure & Dunlop 2004; Vestergaard & Peterson 2006). Note that while the AGNs with the measured reverberation lags and the line width measurements based on the rms spectra have been used to calibrate  $M_{BH}$  estimators, this sample is limited to relatively low- $z$  objects with low-to-moderate luminosity (Bentz et al. 2006). Alternatively, the calibration has been performed by determining the best coefficients in Eq. 1, which provides the most consistent masses compared to  $H\beta$ -based single-epoch masses (e.g., McGill et al. 2008; Shen et al. 2011).

In this work, we present the UV mass estimators by updating the result of McGill et al. (2008), who reported a new calibration of Mg II-based mass estimators using a small sample of 19 AGNs with very high quality Keck spectroscopic data, and investigated the systematic uncertainties due to the variability, line width measurements, and Eddington ratio, which may affect the calibration of UV mass estimators. The improvements of the current work are as follows: (i) the enlarged sample size from 19 AGNs to  $\sim 50$  objects; (ii) the enlarged dynamic range by a factor of  $\sim 2$ ; (iii) the improved and updated spectral decomposition, particularly with a better UV Fe II template; (iv) the updated virial factor and normalization, reflecting the progress of the calibration of  $H\beta$ -based  $M_{BH}$  studies. The high quality spectra from the Keck telescope enable us to reliably remove non-broad line components from the observed spectra to accurately measure the continuum and emission line properties. In §2, we describe the sample, observation, and data reduction. §3 describes the fitting procedure and analysis. §4 presents the calibration. Finally, we provide discussion and summary in §5 and §6, respectively. The following cosmological parameters are used throughout the paper:  $H_0 = 70 \text{ km s}^{-1} \text{ Mpc}^{-1}$ ,  $\Omega_m = 0.30$ , and  $\Omega_\Lambda = 0.70$ .

## 2. OBSERVATIONS & DATA REDUCTION

The sample was initially selected for measuring stellar velocity dispersions of AGN host galaxies to study the evolution of the  $M_{BH} - \sigma_*$  relation (Treu et al. 2004; Woo et al. 2006; Woo 2008; Bennert et al. 2010). We selected moderate luminosity AGNs from SDSS, at particular redshift ranges, at  $\sim 0.36$  and  $\sim 0.52$  in order to observe the broad  $H\beta$  emission line and stellar absorption lines in the rest-frame 5100-5500 Å.

We observed the sample at the Keck telescope between 2003 September and 2009 April as summarized in Table 1 using the Low-Resolution Imaging Spectrometer (Oke et al. 1995), which provided two spectral ranges, containing Mg II (2798Å) and  $H\beta$  (4861Å) broad emission lines at blue and red

CCDs, respectively. The data reduction and calibration for the red and blue CCD data were reported by Woo et al. (2006) and McGill et al. (2008), respectively. Here, we briefly summarize the observations and reduction for the blue CCD. We used the 600 lines  $\text{mm}^{-1}$  grism with a pixel scale of 0.63Å and a resolution of  $145 \text{ km s}^{-1}$  in line dispersion.

Standard spectroscopic data reduction processes, including bias subtraction, flat fielding, flux calibration, and wavelength calibration were performed using IRAF<sup>1</sup>. We extracted one dimensional spectra with a 10 pixel (i.e., 1.35 ") wide aperture. Wavelength calibration was applied using Hg, Ne, Cd arc lamp images. After the flux calibration based on the observation of spectroscopic standard stars (i.e., Feige 34), we rescaled the flux level of our targets to that of SDSS spectrophotometry to compensate the uncertainties of flux calibration due to slit loss, seeing effect, etc. Finally, Galactic extinction was corrected based on the method given by Schlegel et al. (1998) (see Figure 1).

## 3. MEASUREMENTS

We measured the line width of  $H\beta$  and Mg II and the luminosity of the AGN continuum at 5100Å and 3000Å as well as  $H\beta$  and Mg II lines, based on the multi-component spectral analysis (see Table 1). Here, we describe the fitting process for  $H\beta$  and Mg II, respectively.

### 3.1. $H\beta$

To measure the properties of the broad  $H\beta$  line, we performed a multi-component decomposition analysis, following the procedure described by Woo et al. (2006) (see also Woo et al. 2010; Park et al. 2012a; Woo et al. 2013, 2015). All measurements were reported by Park et al. (2015) and here we briefly summarize the fitting procedure for completeness. First, we modeled the AGN continuum with a power-law. The Fe II models were constructed by broadening the I Zw I template from Boroson & Green (1992) with a series of Gaussian velocities, while the stellar component was fitted with a simple stellar population synthesis model of Bruzual & Charlot (2003) with solar metallicity and age of 11 Gyr. The stellar model improves the  $H\beta$  line fitting since the  $H\beta$  absorption line attributed from stellar component is blended with a peak of the  $H\beta$  emission line originated from AGN. In particular, the FWHM of the line profile is sensitive to the shape of the peak while the line dispersion is not significantly affected.

The fitting process was carried out using the non-linear Levenberg-Marquardt least-squares fitting routine `mpfit` (Markwardt 2009) in IDL, using two spectral fitting regions: 4430Å - 4730Å and 5100Å - 5400Å, where the Fe II blends are strong. The blue end of the fitting regions were slightly adjusted to avoid the  $H\gamma$  and  $H\beta$  contamination if necessary.

For the broad component of  $H\beta$ , we used a sixth order Gauss-Hermite series model. If the broad component of  $H\beta$  is blended with the He II  $\lambda 4686$ Å line, we fitted the He II line, using two single Gaussian models, respectively for the broad and narrow components of He II, simultaneously with the  $H\beta$  model. We separately fitted the narrow component of  $H\beta$  using the best-fit model of [O III] 5007Å. Based on the best model of the broad  $H\beta$  component, we measured FWHM,

<sup>1</sup> IRAF is distributed by the National Optical Astronomy Observatories, which are operated by the Association of Universities for Research in Astronomy, Inc., under cooperative agreement with the National Science Foundation (NSF).

TABLE 1  
TARGET PROPERTIES

Name (1)	z (2)	R.A. (3)	Dec. (4)	$i'$ (5)	ut(s) (6)	Run (7)	FWHM $H\beta$ (8)	FWHM $M_{H\beta}$ (9)	$\sigma_{H\beta}$ (10)	$\sigma_{M_{H\beta}}$ (11)	$L_{3000}$ (12)	$L_{5100}$ (13)	$L_{H\beta}$ (14)	$L_{M_{H\beta}}$ (15)
S01	0.3593	153916.24	+032322.07	18.89	10400	1,4	4662 ± 26	3324 ± 66	2194 ± 21	1856 ± 35	2.38 ± 0.01	1.37 ± 0.02	2.22 ± 0.01	5.25 ± 0.05
S02	0.3545	161111.66	+513131.16	19.00	3000	1	4841 ± 35	3332 ± 48	2274 ± 25	2088 ± 35	1.61 ± 0.01	1.25 ± 0.02	2.95 ± 0.01	6.43 ± 0.06
S03	0.3582	173203.08	+611751.89	18.30	5500	1,8	3018 ± 17	2221 ± 42	1716 ± 9	1249 ± 26	4.11 ± 0.01	2.11 ± 0.04	3.80 ± 0.01	4.14 ± 0.04
S04	0.3579	210211.50	-064645.01	18.57	2400	1	2821 ± 46	3079 ± 60	1749 ± 46	1708 ± 45	2.05 ± 0.03	1.19 ± 0.05	1.07 ± 0.02	3.99 ± 0.06
S05	0.3530	210451.83	-071209.41	18.54	12600	1,4	4908 ± 26	4013 ± 114	3333 ± 17	2637 ± 90	3.14 ± 0.09	2.23 ± 0.03	4.52 ± 0.05	6.58 ± 0.14
S06	0.3684	212034.18	-064122.24	18.84	3300	1	4527 ± 65	3056 ± 153	1413 ± 106	1423 ± 123	2.44 ± 0.02	1.10 ± 0.09	1.30 ± 0.04	2.74 ± 0.08
S07	0.3517	230946.14	+000048.87	18.18	7200	1,4	4635 ± 28	3429 ± 125	2547 ± 15	2107 ± 55	3.66 ± 0.03	1.81 ± 0.08	3.89 ± 0.01	3.50 ± 0.05
S08	0.3585	235953.44	-093655.63	18.49	2400	1	2909 ± 63	2212 ± 72	1217 ± 33	1167 ± 75	2.89 ± 0.02	1.59 ± 0.05	0.89 ± 0.03	1.70 ± 0.05
S09	0.3542	005916.10	+153816.10	18.38	1800	1	2655 ± 28	2946 ± 52	1749 ± 21	1652 ± 44	2.68 ± 0.03	1.76 ± 0.06	2.80 ± 0.03	6.74 ± 0.08
S10	0.3505	010112.06	-094500.81	17.97	3300	1,7	4850 ± 20	3388 ± 97	2597 ± 12	2034 ± 96	6.65 ± 0.06	2.77 ± 0.04	6.12 ± 0.02	6.84 ± 0.11
S11	0.3558	010715.97	-083429.37	18.47	10200	1,4	2595 ± 14	2650 ± 50	1354 ± 8	1410 ± 39	3.33 ± 0.05	1.57 ± 0.03	2.55 ± 0.01	2.74 ± 0.04
S12	0.3574	021340.59	+134756.05	18.37	1800	1	8800 ± 333	7014 ± 172	4256 ± 56	3376 ± 107	3.58 ± 0.05	1.82 ± 0.12	4.67 ± 0.03	8.30 ± 0.13
S16	0.3702	111937.59	+005620.36	19.10	600	9	3749 ± 784	7008 ± 704	1867 ± 445	3518 ± 579	0.21 ± 0.02	0.69 ± 0.11	0.76 ± 0.08	0.41 ± 0.03
S21	0.3532	110536.18	+031243.15	17.31	1500	2	8296 ± 145	4311 ± 211	1897 ± 105	2037 ± 131	1.92 ± 0.01	5.33 ± 0.09	8.10 ± 0.03	2.36 ± 0.05
S23	0.3511	140016.65	-010822.16	18.16	1800	2,4	9629 ± 146	5482 ± 151	4251 ± 168	2604 ± 55	2.20 ± 0.01	1.78 ± 0.03	2.70 ± 0.02	4.63 ± 0.05
S24	0.3616	140034.70	+004733.43	18.29	9600	2,4	7061 ± 49	4466 ± 72	2635 ± 17	2288 ± 30	1.81 ± 0.03	1.49 ± 0.02	2.39 ± 0.01	5.00 ± 0.03
S26	0.3691	152922.26	+592854.54	18.92	3600	2	5386 ± 22	4642 ± 149	1914 ± 10	2305 ± 130	1.59 ± 0.01	0.83 ± 0.02	2.36 ± 0.02	2.43 ± 0.06
S27	0.3667	153651.27	+541442.63	18.86	7200	2	2508 ± 28	2682 ± 65	1409 ± 17	1234 ± 47	1.52 ± 0.04	1.26 ± 0.05	1.72 ± 0.01	1.88 ± 0.03
S28	0.3679	161136.29	+451610.91	18.63	5760	3,4	4600 ± 51	4974 ± 87	2532 ± 36	2690 ± 47	2.06 ± 0.02	0.97 ± 0.03	1.79 ± 0.02	4.43 ± 0.04
S29	0.3575	215841.92	-011500.32	18.95	3600	3	3533 ± 44	3036 ± 72	1847 ± 28	1780 ± 57	1.14 ± 0.02	1.20 ± 0.04	1.48 ± 0.01	1.59 ± 0.02
S31	0.3505	101527.26	+625911.52	18.15	9000	9,10	4012 ± 27	3099 ± 123	2117 ± 20	1887 ± 74	1.75 ± 0.02	0.93 ± 0.03	2.24 ± 0.01	1.93 ± 0.04
S31	0.3566	080427.98	+522306.21	18.55	9000	5	2620 ± 49	2458 ± 79	1501 ± 32	1255 ± 66	1.59 ± 0.02	1.04 ± 0.08	1.88 ± 0.03	1.62 ± 0.03
S32	0.3672	093455.60	+051409.15	18.82	7200	5	2815 ± 61	2777 ± 61	1316 ± 41	1296 ± 46	0.90 ± 0.01	0.83 ± 0.04	0.81 ± 0.02	0.97 ± 0.02
S34	0.3630	095850.15	+400342.33	18.74	5400	9	2213 ± 35	2302 ± 29	1378 ± 15	1198 ± 21	2.28 ± 0.01	1.35 ± 0.05	1.93 ± 0.01	3.83 ± 0.03
S35	0.3733	100706.25	+084228.41	18.69	3600	9	2790 ± 63	1954 ± 83	1612 ± 40	1092 ± 65	1.39 ± 0.01	1.40 ± 0.04	0.90 ± 0.01	0.49 ± 0.02
S36	0.3584	102103.57	+304755.87	18.92	5400	9	1947 ± 21	2069 ± 86	1031 ± 13	868 ± 57	1.33 ± 0.01	0.69 ± 0.03	1.12 ± 0.01	0.85 ± 0.02
S37	0.3618	104331.50	-010732.88	18.82	5400	9	2959 ± 56	2020 ± 79	1371 ± 27	1163 ± 47	2.06 ± 0.01	0.98 ± 0.04	1.19 ± 0.01	1.44 ± 0.03
S38	0.3656	104610.60	+035031.26	18.45	9900	9,10,11	2733 ± 43	2446 ± 48	1532 ± 11	1298 ± 28	3.20 ± 0.01	1.54 ± 0.02	2.27 ± 0.01	3.03 ± 0.03
S39	0.3701	125838.71	+455515.55	18.56	5400	9	2787 ± 27	3014 ± 50	1569 ± 14	1501 ± 25	2.87 ± 0.04	1.25 ± 0.02	2.08 ± 0.02	4.25 ± 0.04
S39	0.3701	125838.71	+455515.55	18.56	5400	9	2787 ± 27	3014 ± 50	1569 ± 14	1501 ± 25	2.87 ± 0.04	1.25 ± 0.02	2.08 ± 0.02	4.25 ± 0.04
S39	0.3701	125838.71	+455515.55	18.56	5400	9	2787 ± 27	3014 ± 50	1569 ± 14	1501 ± 25	2.87 ± 0.04	1.25 ± 0.02	2.08 ± 0.02	4.25 ± 0.04
S39	0.3701	125838.71	+455515.55	18.56	5400	9	2787 ± 27	3014 ± 50	1569 ± 14	1501 ± 25	2.87 ± 0.04	1.25 ± 0.02	2.08 ± 0.02	4.25 ± 0.04
S39	0.3701	125838.71	+455515.55	18.56	5400	9	2787 ± 27	3014 ± 50	1569 ± 14	1501 ± 25	2.87 ± 0.04	1.25 ± 0.02	2.08 ± 0.02	4.25 ± 0.04
S39	0.3701	125838.71	+455515.55	18.56	5400	9	2787 ± 27	3014 ± 50	1569 ± 14	1501 ± 25	2.87 ± 0.04	1.25 ± 0.02	2.08 ± 0.02	4.25 ± 0.04
S39	0.3701	125838.71	+455515.55	18.56	5400	9	2787 ± 27	3014 ± 50	1569 ± 14	1501 ± 25	2.87 ± 0.04	1.25 ± 0.02	2.08 ± 0.02	4.25 ± 0.04
S39	0.3701	125838.71	+455515.55	18.56	5400	9	2787 ± 27	3014 ± 50	1569 ± 14	1501 ± 25	2.87 ± 0.04	1.25 ± 0.02	2.08 ± 0.02	4.25 ± 0.04
S39	0.3701	125838.71	+455515.55	18.56	5400	9	2787 ± 27	3014 ± 50	1569 ± 14	1501 ± 25	2.87 ± 0.04	1.25 ± 0.02	2.08 ± 0.02	4.25 ± 0.04
S39	0.3701	125838.71	+455515.55	18.56	5400	9	2787 ± 27	3014 ± 50	1569 ± 14	1501 ± 25	2.87 ± 0.04	1.25 ± 0.02	2.08 ± 0.02	4.25 ± 0.04
S39	0.3701	125838.71	+455515.55	18.56	5400	9	2787 ± 27	3014 ± 50	1569 ± 14	1501 ± 25	2.87 ± 0.04	1.25 ± 0.02	2.08 ± 0.02	4.25 ± 0.04
S39	0.3701	125838.71	+455515.55	18.56	5400	9	2787 ± 27	3014 ± 50	1569 ± 14	1501 ± 25	2.87 ± 0.04	1.25 ± 0.02	2.08 ± 0.02	4.25 ± 0.04
S39	0.3701	125838.71	+455515.55	18.56	5400	9	2787 ± 27	3014 ± 50	1569 ± 14	1501 ± 25	2.87 ± 0.04	1.25 ± 0.02	2.08 ± 0.02	4.25 ± 0.04
S39	0.3701	125838.71	+455515.55	18.56	5400	9	2787 ± 27	3014 ± 50	1569 ± 14	1501 ± 25	2.87 ± 0.04	1.25 ± 0.02	2.08 ± 0.02	4.25 ± 0.04
S39	0.3701	125838.71	+455515.55	18.56	5400	9	2787 ± 27	3014 ± 50	1569 ± 14	1501 ± 25	2.87 ± 0.04	1.25 ± 0.02	2.08 ± 0.02	4.25 ± 0.04
S39	0.3701	125838.71	+455515.55	18.56	5400	9	2787 ± 27	3014 ± 50	1569 ± 14	1501 ± 25	2.87 ± 0.04	1.25 ± 0.02	2.08 ± 0.02	4.25 ± 0.04
S39	0.3701	125838.71	+455515.55	18.56	5400	9	2787 ± 27	3014 ± 50	1569 ± 14	1501 ± 25	2.87 ± 0.04	1.25 ± 0.02	2.08 ± 0.02	4.25 ± 0.04
S39	0.3701	125838.71	+455515.55	18.56	5400	9	2787 ± 27	3014 ± 50	1569 ± 14	1501 ± 25	2.87 ± 0.04	1.25 ± 0.02	2.08 ± 0.02	4.25 ± 0.04
S39	0.3701	125838.71	+455515.55	18.56	5400	9	2787 ± 27	3014 ± 50	1569 ± 14	1501 ± 25	2.87 ± 0.04	1.25 ± 0.02	2.08 ± 0.02	4.25 ± 0.04
S39	0.3701	125838.71	+455515.55	18.56	5400	9	2787 ± 27	3014 ± 50	1569 ± 14	1501 ± 25	2.87 ± 0.04	1.25 ± 0.02	2.08 ± 0.02	4.25 ± 0.04
S39	0.3701	125838.71	+455515.55	18.56	5400	9	2787 ± 27	3014 ± 50	1569 ± 14	1501 ± 25	2.87 ± 0.04	1.25 ± 0.02	2.08 ± 0.02	4.25 ± 0.04
S39	0.3701	125838.71	+455515.55	18.56	5400	9	2787 ± 27	3014 ± 50	1569 ± 14	1501 ± 25	2.87 ± 0.04	1.25 ± 0.02	2.08 ± 0.02	4.25 ± 0.04
S39	0.3701	125838.71	+455515.55	18.56	5400	9	2787 ± 27	3014 ± 50	1569 ± 14	1501 ± 25	2.87 ± 0.04	1.25 ± 0.02	2.08 ± 0.02	4.25 ± 0.04
S39	0.3701	125838.71	+455515.55	18.56	5400	9	2787 ± 27	3014 ± 50	1569 ± 14	1501 ± 25	2.87 ± 0.04	1.25 ± 0.02	2.08 ± 0.02	4.25 ± 0.04
S39	0.3701	125838.71	+455515.55	18.56	5400	9	2787 ± 27	3014 ± 50	1569 ± 14	1501 ± 25	2.87 ± 0.04	1.25 ± 0.02	2.08 ± 0.02	4.25 ± 0.04
S39	0.3701	125838.71	+455515.55	18.56	5400	9	2787 ± 27	3014 ± 50	1569 ± 14	1501 ± 25	2.87 ± 0.04	1.25 ± 0.02	2.08 ± 0.02	4.25 ± 0.04
S39	0.3701	125838.71	+455515.55	18.56	5400	9	2787 ± 27	3014 ± 50	1569 ± 14	1501 ± 25	2.87 ± 0.04	1.25 ± 0.02	2.08 ± 0.02	4.25 ± 0.04
S39	0.3701	125838.71	+455515.55	18.56	5400	9	2787 ± 27	3014 ± 50	1569 ± 14	1501 ± 25	2.87 ± 0.04	1.25 ± 0.02	2.08 ± 0.02	4.25 ± 0.04
S39	0.3701	125838.71	+455515.55	18.56	5400	9	2787 ± 27	3014 ± 50	1569 ± 14	1501 ± 25	2.87 ± 0.04	1.25 ± 0.02	2.08 ± 0.02	4.25 ± 0.04
S39	0.3701	125838.71	+455515.55	18.56	5400	9	2787 ± 27	3014 ± 50	1569 ± 14	1501 ± 25	2.87 ± 0.04	1.25 ± 0.02	2.08 ± 0.02	4.25 ± 0.04
S39	0.3701	125838.71	+455515.55	18.56	5400	9	2787 ± 27	3014 ± 50	1569 ± 14	1501 ± 25	2.87 ± 0.04	1.25 ± 0.02	2.08 ± 0.02	4.25 ± 0.04
S39	0.3701	125838.71	+455515.55	18.56	5400	9	2787 ± 27	3014 ± 50	1569 ± 14	1501 ± 25	2.87 ± 0.04	1.25 ± 0.02	2.08 ± 0.02	4.25 ± 0.04
S39	0.3701	125838.71	+455515.55	18.56	5400	9	2787 ± 27	3014 ± 50	1569 ± 14	1501 ± 25	2.87 ± 0.04	1.25 ± 0.02	2.08 ± 0.02	4.25 ± 0.04
S39	0.3701	125838.71	+455515.55	18.56	5400	9	2787 ± 27	3014 ± 50	1569 ± 14	1501 ± 25	2.87 ± 0.04	1.25 ± 0.02	2.08 ± 0.02	4.25 ± 0.04
S39	0.3701	125838.71	+455515.55	18.56	5400	9	2787 ± 27	3014 ± 50	1569 ± 14	1501 ± 25	2.87 ± 0.04	1.25 ± 0.02	2.08 ± 0.02	4.25 ± 0.04
S39	0.3701	125838.71	+455515.55	18.56	5400	9	2787 ± 27	3014 ± 50	1569 ± 14	1501 ± 25	2.87 ± 0.04	1.25 ± 0.02	2.08 ± 0.02	4

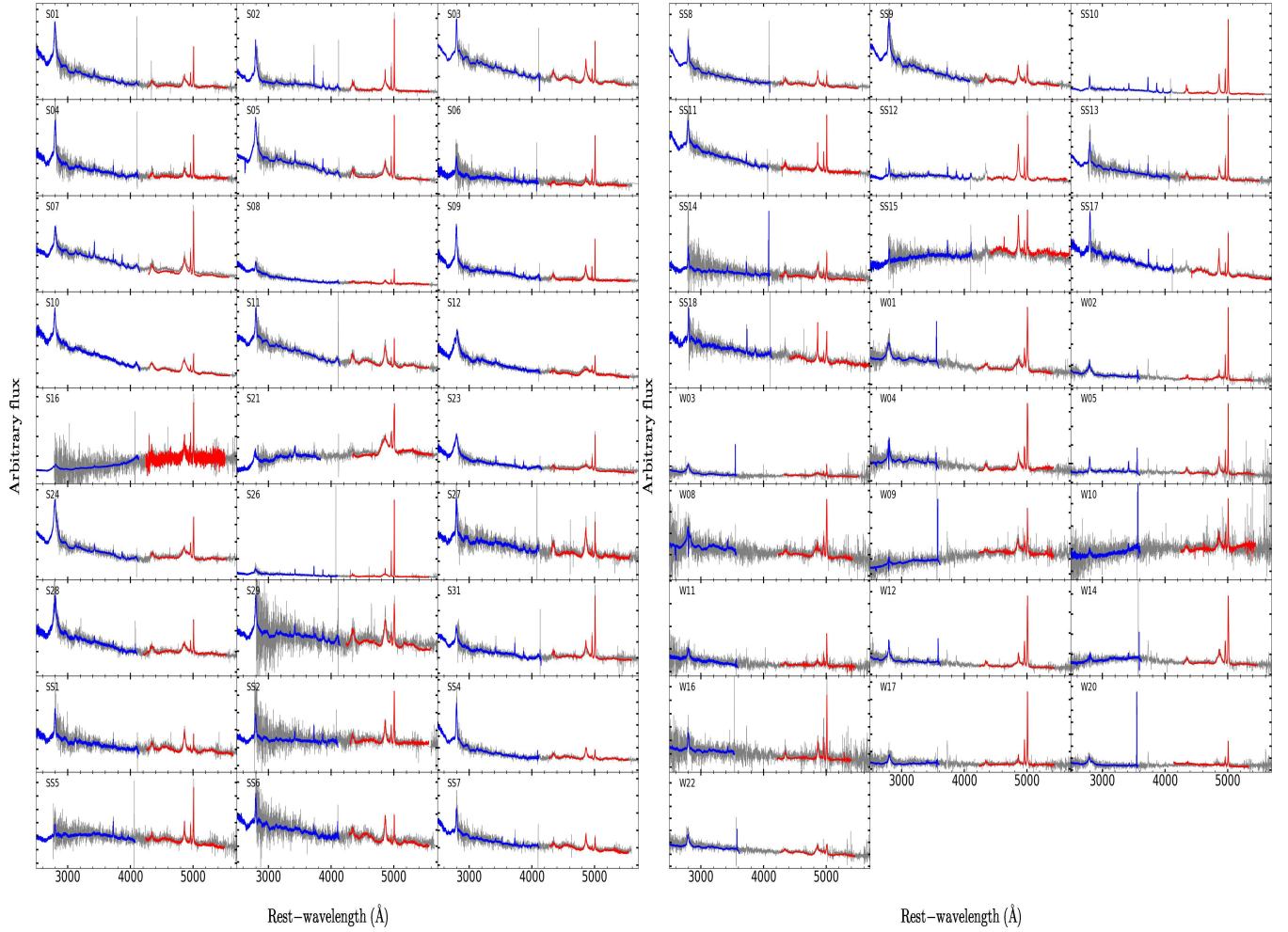


FIG. 1.— Rest-frame spectra, covering the Mg II (blue) and the H $\beta$  regions (red) obtained with Keck LRIS. The SDSS spectra after Galactic extinction correction are shown in gray.

TABLE 2  
OBSERVATION LOG

Run	Date	Slit (arcsec)	Seeing (arcsec)	Weather
(1)	(2)	(3)	(4)	(5)
1	2003 Sep 3	1.5	$\sim 1$	Cirrus
2	2004 May 14	1	$\sim 1$	Cirrus
3	2004 May 22	1	$\sim 0.8$	Clear
4	2005 Jul 7,8	1	$\sim 0.7-0.9$	Clear
5	2007 Jan 23,24,25	1	$\sim 0.6-1.2$	Clear
6	2007 Apr 19,20,21	1	$\sim 0.6-0.8$	Clear
7	2007 Aug 18,19	1	$\sim 1-1.7$	Clear
8	2008 Aug 2,3	1	$\sim 0.8$	Clear
9	2009 Jan 21,22	1	$\sim 1.1-1.5$	Clear
10	2009 Apr 2	1	$\sim 1.2$	Cirrus
11	2009 Apr 16	1	$\sim 0.8$	Clear

NOTE. — Col. (1): Observing run. Col. (2): Observing date. Col. (3): Slit width. Col. (4): Seeing. Col. (5): weather condition

line dispersion ( $\sigma_{H\beta}$ ), and line luminosity. We also measured the monochromatic luminosity at  $5100\text{\AA}$  ( $L_{5100}$ ) by averaging the continuum flux in the  $50\text{\AA}$  window, using the power-law model representing the AGN continuum. The measurement errors of the line width and continuum luminosity were determined based on the Monte Carlo simulations by generating 100 mock spectra by randomly fluctuating fluxes using the flux errors, and performing the decomposition analysis for each spectrum. We used the  $1\text{-}\sigma$  dispersion of the distribution as the measurement uncertainty.

### 3.2. Mg II

For measuring the width and luminosity of the Mg II line, we followed the procedure outlined by McGill et al. (2008). The multi-component fitting procedure is similar to that applied to the  $H\beta$  region, and here we briefly describe the fitting process. First, we fitted AGN power-law continuum and Fe II blends, using the two windows:  $2600\text{\AA} - 2750\text{\AA}$  and  $2850\text{\AA} - 3090\text{\AA}$ . Second, we fitted the Mg II line with a sixth order Gauss-Hermite series. The purpose of the line fitting is to measure the flux-weighted width of the line profile, for representing the velocity distribution of the gas. Thus, while we do not attempt to interpret the meaning of each coefficient in the Gauss-Hermite series, we determine the best model to reproduce the line profile. Since the Gauss-Hermite series can have negative values at the wing of the line profile, we empirically limit or adjust the fitting range, in order to prevent negative fluxes in the best-fit model.

We decided not to use a separate model to fit a narrow component of Mg II since we do not see a clear signature that suggests the presence of the narrow component in the Mg II line profile (see § 5.1 for more details on the narrow component subtraction). Note that the FWHM measurements of the broad Mg II can be underestimated if the existing narrow component in Mg II is not subtracted, while the effect on the line dispersion measurements will be insignificant. Several objects show strong absorption features in the Mg II line profile (e.g., W04, W08, W09, W14), for which we applied Gaussian models and simultaneously fitted them with the Mg II line profile. When the absorption features are close to the line center, increasing the uncertainty of the line width measurements, we checked whether the uncertainties of these objects introduces any systematic trend and found no significant effect (see Section 4.1). Third, the measurement errors of the Mg II line width and the continuum luminosity at  $3000\text{\AA}$  were determined based on the Monte Carlo simulations. By randomly fluctuating fluxes using the flux errors, we generated 100 mock spectra and performed the decomposition analysis for each spectrum. Then, the  $1\text{-}\sigma$  dispersion of the distribution was taken as the measurement uncertainty.

As investigated by Wang et al. (2009), a careful treatment is required for fitting Fe II blends in the Mg II region. We used the Fe II template from Vestergaard & Wilkes (2001) in our previous study (McGill et al. 2008). However, this template contains no information of Fe II underneath the Mg II line because it was constructed from the observed spectrum of the narrow line Seyfert 1 galaxy, I Zwicky 1 after masking the Mg II line. Instead, Tsuzuki et al. (2006) suggested a new template calculated based on the one dimensional photoionization model combined with the observed spectrum of I Zw 1. The merit of this template is that the Fe II emission at the location of Mg II is available. Thus, we investigated the difference of the line fitting results using the two different

templates.

In Figure 2 we present an example of the best-fit results based on the Fe II templates of Vestergaard & Wilkes (2001) (blue) and Tsuzuki et al. (2006) (red), respectively, for one AGN from our sample. There is a clear difference between the two fitting results: the best-fit Mg II line profile is broader and stronger when the template of Vestergaard & Wilkes (2001) was used. This is due to the fact that there is no Fe II flux underneath of Mg II in Vestergaard & Wilkes (2001) template, hence, the Mg II line model takes more flux from the blended region (i.e., close to the wing of Mg II) into the Mg II line flux. Thus, in the following analysis, we will use the results based on the Fe II template of Tsuzuki et al. (2006) for UV mass estimators.

Note that the template mismatch in subtracting the Fe II blends may cause additional systematic errors on the line width measurements. Wang et al. (2009) reported that the revised Fe II template by Tsuzuki et al. (2006) can provide reliable measurements within a 20% uncertainty in the case of Mg II FWHM with the SDSS quality data. Thus, we expect that the uncertainty due to the template mismatch would be even smaller than 20% for given high quality of our Keck data. Considering the possibility that the errors based on the Monte Carlo simulation underestimate the true uncertainty of the line width measurements, we assume an average error of 5%, 10%, and 20%, respectively, in comparing the Mg II line width with that of  $H\beta$ . We find that regardless of the adopted errors, the best-fit slopes are consistent among each other, indicating that the fitting results are independent of the width measurement errors, unless the uncertainty is significantly larger than 20%. Also, we investigate how the larger errors of the line width measurements affect the calibration of the best mass estimators. We obtain consistent results regardless of the adopted errors while the intrinsic scatter between mass estimates decreases with the increasing measurement errors as expected (see Section 4.3.2).

The best-fit results for the Mg II line region based on the Fe II template by Tsuzuki et al. (2006) are presented in Figure 3, while the multicomponent fitting results for the  $H\beta$  region were presented by Park et al. (2015). There are several objects with relatively strong internal extinction, namely, S16, S21, SS15, W09, W10, for which the spectral slope is very different compared to that of other AGNs in Figure 1. Thus, we will exclude these five AGNs from the  $M_{BH}$  estimator calibration since the luminosity and line width measurements are uncertain without a proper extinction correction. There are a couple of other AGNs with a hint of internal extinction in the Mg II region (e.g., SS5, SS12, W14), however, we decided to exclude only the five objects based on the spectral shape in the total UV to optical range (see more discussion in § 4.2).

### 3.3. Comparison of line profiles

We directly compare the best-fit model of the  $H\beta$  and Mg II line profiles after normalizing the flux with the peak value in Figure 4. While the majority of objects shows a similar line profiles between  $H\beta$  and Mg II, the  $H\beta$  width is somewhat broader than that of Mg II, as previously reported. For example, Marziani et al. (2013) showed that on average  $H\beta$  is 20% broader than Mg II. However, there are cases with a much larger difference in their line profiles. In the case of S21, S24, S23, W02, W03, W09, W12, W20, the  $H\beta$  line profile is clearly different from that of Mg II and the line width of  $H\beta$  is much broader than that of Mg II by more than a factor of  $\sim$ two. Note that this discrepancy is mainly observed in AGNs

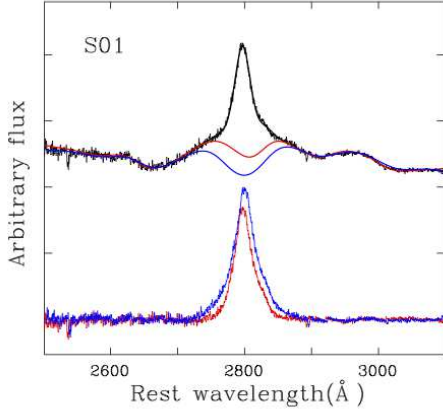


FIG. 2.— Top: The raw spectrum of S01 is shown (black) along with the best-fit Fe II models, respectively, using the Fe II templates from Vestergaard & Wilkes 2001 (blue) and Tsuzuki et al. 2006 (red). Bottom: Fe II-subtracted Mg II line profiles are presented, using the two different Fe II templates.

with a very broad  $H\beta$  line (see the discussion on population A in Marziani et al. 2013). In contrast, we found that one object, S16 shows a much broader line in Mg II than in  $H\beta$  by a factor of  $\sim 1.8$ . It is not clear why the line profiles are very different between  $H\beta$  and Mg II. For the purpose of this study, we will compare the line width of  $H\beta$  and Mg II to provide UV mass estimators. However, it is clear that the  $M_{BH}$  based on the Mg II line will be systematically different for these objects. If we assume that the  $H\beta$ -based mass represents the true  $M_{BH}$ , then Mg II-based mass will suffer from systematic uncertainties due to the intrinsic difference of the line profiles between  $H\beta$  and Mg II. Thus, we will investigate the effect of these AGNs (six objects after excluding S16 and S21 due to heavy extinction) in our mass calibration (see § 4.3).

To understand the characteristics of the line profiles, we compare line dispersion and FWHM of Mg II, using the measurements based on the template of Tsuzuki et al. (2006) (Figure 5 left). The average ratio between FWHM and line dispersion of Mg II is  $\langle \log FWHM/\sigma \rangle = 0.27 \pm 0.05$ , corresponding to 1.86 in linear scale, which is smaller than 2.36, the ratio of a Gaussian profile. The linear regression between FWHM and line dispersion ( $\sigma$ ) of Mg II shows a slope of  $0.90 \pm 0.04$ , indicating that FWHM and line dispersion shows almost linear relationship. In other words, the shape of the line profile of Mg II does not significantly change as a function of the line width although there is a slight hint that broader Mg II lines tend to have broader wings and narrower core than narrower Mg II lines.

In the case of  $H\beta$ , the FWHM-to-line dispersion ratio is  $\sim 2$  with a scatter larger than a factor of 2. Also, the ratio increases with increasing line width, suggesting that there may be a systematic difference in the line profile between AGNs with a very broad line and AGNs with a relatively narrow line. In contrast, the FWHM/ $\sigma$  ratio of Mg II is similar to that of  $H\beta$ , but with a much smaller scatter, indicating the Mg II line may not suffer a strong systematic trend as a function of the line width.

#### 4. CALIBRATION

In this section we perform correlation analysis, respectively for line widths (§ 4.1), luminosities (§ 4.2), and  $M_{BH}$  esti-

mates (§ 4.3), and present the best-fit results. For the regression, we use the FITEXY method as implemented by Park et al. (2012b) using MPFIT (Markwardt 2009), which finds the best-fit parameters (intercept, slope and intrinsic scatter  $\sigma_{int}$ ) by minimizing a reduced  $\chi^2$ , after accounting for the measurement errors (see the detailed descriptions in Park et al. 2012b). From the Keck sample, we exclude five objects with strong internal extinction, namely, S16, SS15, S21, W09, and W10 as we described in Section 3.2, since the measured luminosities and line velocities are biased.

##### 4.1. Line width comparison

We compared the width measurements of Mg II with those of  $H\beta$  in Figure 6. As the line profile of Mg II is often different from that of  $H\beta$  as shown in Figure 4, we assumed an intrinsic scatter between the widths of the two lines in the fitting process. While we measured the uncertainty of the line width measurements based on the Monte Carlo simulations as discussed in Section 3.2, we also considered the systematic uncertainty and tested the fitting results assuming an average error of 5%, 10%, and 20%, respectively, as the uncertainty of the width measurements of the Mg II line. We found that regardless of the adopted errors, the best-fit slopes are consistent among each other, indicating that the fitting results are independent of the width measurement errors, unless the uncertainty is significantly large ( $> 20\%$ ). For the final fitting results, we used the errors measured from the Monte Carlo simulations.

First, we compared  $H\beta$  line width and Mg II line width, that was measured from the spectral decomposition based on the Fe II template of Tsuzuki et al. (2006) (top panels in Figure 6). We obtained the best-fit result as

$$\log(\sigma_{MgII}) \propto 0.84 \pm 0.07 \times \log(\sigma_{H\beta}), \quad (2)$$

with  $\sigma_{int} = 0.08 \pm 0.01$ , indicating a sub-linear relationship that Mg II is somewhat narrower than  $H\beta$ , particularly for AGNs with a broader line. In the case of FWHM, we obtained a shallower slope,

$$\log(FWHM_{MgII}) \propto 0.60 \pm 0.07 \times \log(FWHM_{H\beta}), \quad (3)$$

with  $\sigma_{int} = 0.09 \pm 0.01$ . To investigate this correlation further, we adopted a sample of 495 SDSS AGNs with  $S/N \geq 20$  for Mg II and  $H\beta$  from Wang et al. (2009), who used the same Fe II template of Tsuzuki et al. (2006) in modeling the Mg II line profile, and measured FWHM of Mg II and  $H\beta$ . For the combined sample of the Keck and SDSS AGNs, we obtained the best-fit slope of  $0.72 \pm 0.03$  ( $\sigma_{int} = 0.04 \pm 0.01$ ), which is higher than that we obtained using the Keck sample only. Since Wang et al. (2009) modeled the Mg II line profile after subtracting a narrow component of Mg II, it is possible that some of the FWHM measurements are systematically overestimated.

To investigate the systematic effect due to the choice of the Fe II template, we also used Mg II line width measurements based on the Fe II template of Vestergaard & Wilkes (2001) (bottom panels in Figure 6). As described in Section 3.2, the subtraction using the template from Vestergaard & Wilkes (2001) introduces systematic uncertainties due to the lack of Fe II features at the location of the Mg II line. We found a more significant systematic difference of the line dispersions between Mg II and  $H\beta$  with the best-fit slope of  $0.53 \pm 0.05$  ( $\sigma_{int} = 0.06 \pm 0.01$ ). These results support the hypothesis that the Fe II template of Vestergaard & Wilkes (2001) introduces additional systematic uncertainties on the line width



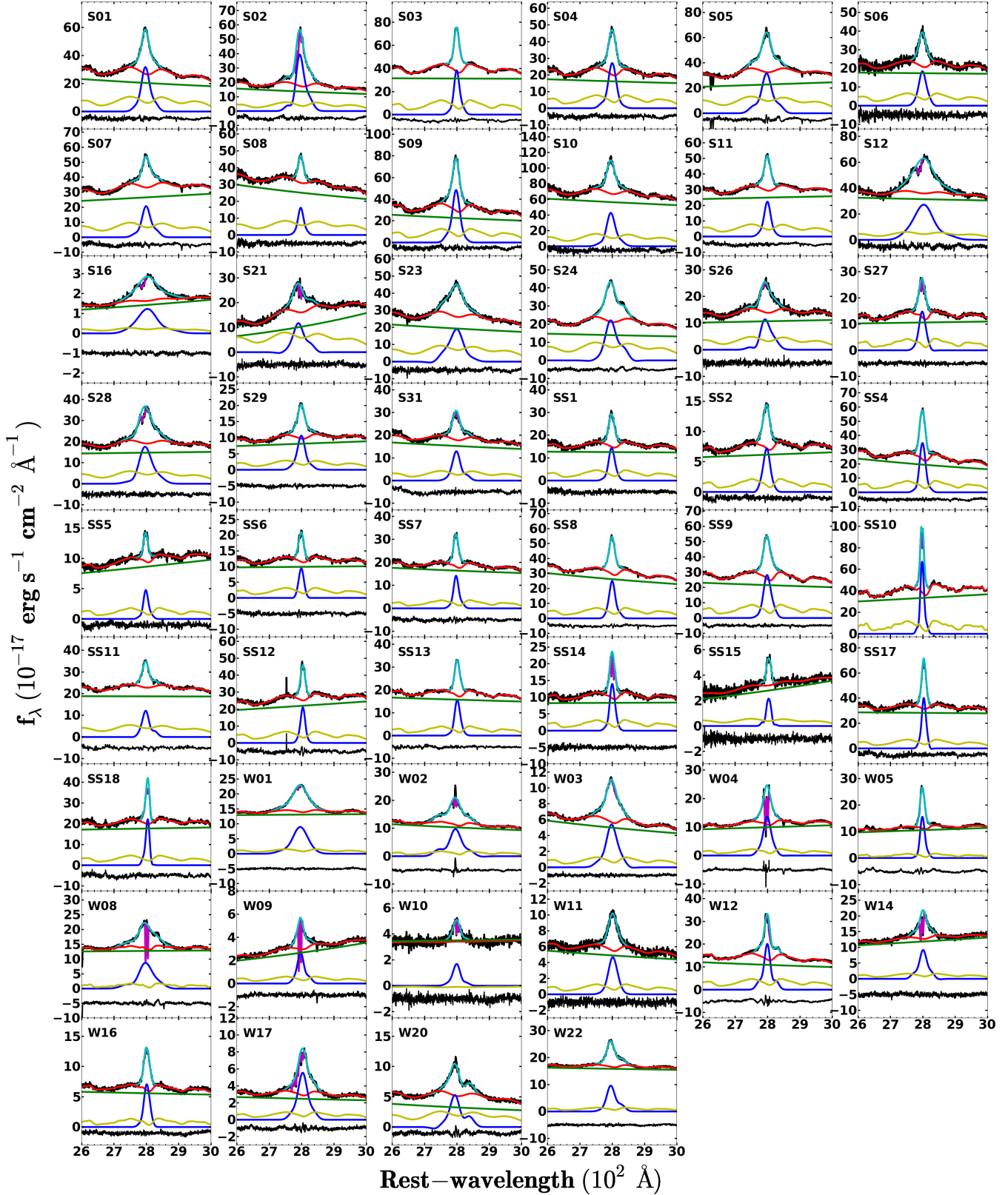


FIG. 3.— Multi-component fitting results for the Mg II emission line region, using the Fe II template of Tsuzuki et al. (2006). In each panel, the rest-frame Keck spectrum (thick black), power-law continuum + Fe II model (red), total model including Mg II (cyan), and models for the absorption line features in Mg II (magenta) are presented in the top, while the best-fit pseudo-continuum, i.e., AGN power-law continuum (green) and Fe II model (yellow), and the Mg II line model (blue) are presented in the middle. In the bottom, the residual (black) between the observed spectrum and the combined models is shown, after shifting it down arbitrarily for clarity.



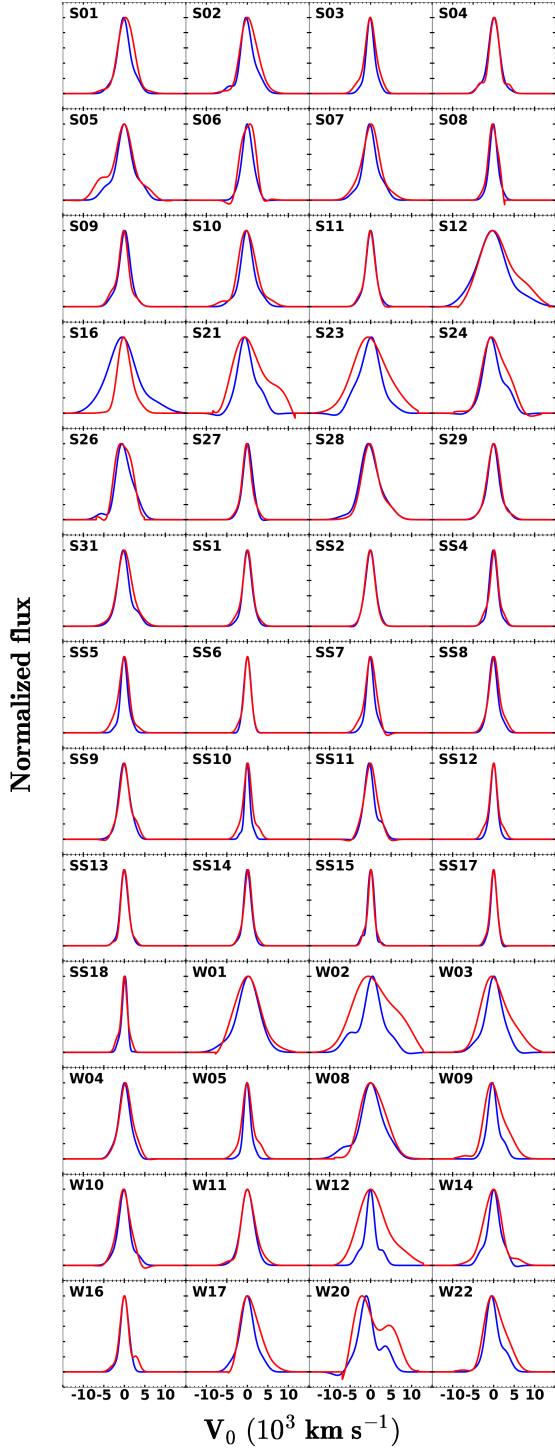


FIG. 4.— Comparison of the best-fit model profiles of Mg II (blue) and H $\beta$  (red) line profiles. The flux is normalized for comparison.

measurements, particularly for the line dispersion. In the case of FWHM between Mg II and H $\beta$ , we obtained the best-fit slope  $0.55 \pm 0.06$  ( $\sigma_{\text{int}} = 0.07 \pm 0.01$ ), which is similar to the slope  $0.60 \pm 0.07$ , that we obtained using the Keck sample based on the Tsuzuki et al. (2006) template, indicating that the choice of Fe II template makes less significant difference in comparing the FWHM of Mg II and H $\beta$ . We also adopted the FWHM measurements from Shen et al. (2011), who used the Fe II template of Vestergaard & Wilkes (2001) for the Mg II

line fitting process for a large sample of type 1 AGNs, by selecting 6017 AGNs at  $0.4 \leq z \leq 0.8$  with  $S/N \geq 10$  in the continuum (4750–4950 Å). Using the combined sample of the Keck and SDSS AGNs, we obtained the best-fit slope  $0.75 \pm 0.01$  ( $\sigma_{\text{int}} = 0.08 \pm 0.01$ ), which is again close to the slope that we obtained using the measurements of Mg II FWHM from Wang et al. (2009) based on the template of Tsuzuki et al. (2006). These results suggest that the choice of Fe II template does not strongly affect the FWHM comparison, while it strongly changes the correlation between the line dispersions of Mg II and H $\beta$  as expected from the fact that the two templates make a significant difference in the wing of the Mg II line profile.

#### 4.2. Luminosity comparison

We compare various continuum and line luminosities with the best calibrated continuum luminosity at 5100 Å ( $L_{5100}$ ), in order to use the UV luminosities as a proxy for BLR size. Note that including or excluding the six AGNs with very different line profiles between Mg II and H $\beta$  does not significantly change the result. Thus, we only present the best-fit result including these AGNs. First, we compare  $L_{5100}$  with  $L_{H\beta}$  for the Keck sample, obtaining the best-fit slope  $1.03 \pm 0.08$  with  $\sigma_{\text{int}} = 0.18 \pm 0.02$ . This result is consistent with but slightly shallower than the slope  $1.13 \pm 0.01$  reported by Greene & Ho (2005). In order to increase the dynamic range, we adopted the measurements of 6017 SDSS AGNs from Shen et al. (2011), which were used for the line width comparison in § 4.1. For this comparison, we made an arbitrary luminosity cut at  $\log(L_{H\beta}) = 42.7$  and  $\log(L_{5100}) = 44.5$  for further selecting 4584 luminous AGNs, in order to avoid uncertain  $L_{5100}$  measurements of lower luminosity AGNs since the potential contribution from stellar continuum can be significant. In fact, a systematic offset at low luminosity is clearly present in Figure 7 (grey points). By combining our Keck sample and the higher luminosity SDSS AGNs, we obtained the best-fit result,

$$\log(L_{H\beta}) \propto 0.99 \pm 0.01 \times \log(L_{5100}), \quad (4)$$

with  $\sigma_{\text{int}} = 0.15 \pm 0.01$ , again consistent with the linear relationship.

Second, by comparing  $L_{3000}$  with  $L_{5100}$ , we obtained the best-fit slope  $0.74 \pm 0.06$  ( $\sigma_{\text{int}} = 0.12 \pm 0.01$ ) for the Keck sample. To increase the dynamic range, we also adopted 4800 luminous AGNs from Shen et al. (2011), using the luminosity cut at  $\log(L_{3000}) = 42.62$  and  $\log(L_{5100}) = 45.5$ , to avoid the systematic uncertainty due to stellar contribution to  $L_{5100}$ . In this case we obtained the best-fit result,

$$\log(L_{3000}) \propto 1.06 \pm 0.01 \times \log(L_{5100}), \quad (5)$$

with  $\sigma_{\text{int}} = 0.10 \pm 0.01$ .

Third, by comparing the  $L_{\text{MgII}}$  with  $L_{5100}$ , we obtained the best-fit slope  $0.62 \pm 0.13$  ( $\sigma_{\text{int}} = 0.24 \pm 0.03$ ) based on the Keck sample (bottom left in Figure 7). If we combined the Keck sample with the SDSS AGNs from Wang et al. (2009), who used the same Fe II template for the Mg II line fitting, we obtained the best-fit result,

$$\log(L_{\text{MgII}}) \propto 0.87 \pm 0.03 \times \log(L_{5100}), \quad (6)$$

with  $\sigma_{\text{int}} = 0.20 \pm 0.01$ . The sub-linear correlation between Mg II and UV continuum luminosities represents the Baldwin effect (Baldwin 1977), which can be explained due to the increase of the thermal component in the UV continuum,

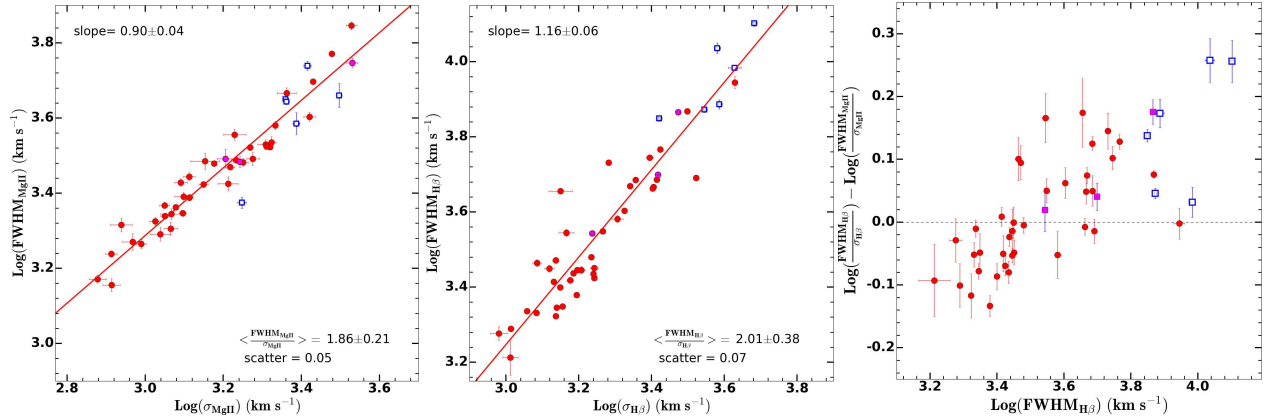


FIG. 5.— Comparing the FWHM and line dispersion ( $\sigma$ ) of Mg II (left) and  $H\beta$  (center). The objects with strong absorption line features in the Mg II line are denoted as magenta squares, showing that these objects are not deviating from the distribution of other AGNs. The six AGNs with strong discrepancy of line profiles between  $H\beta$  and Mg II are shown as open blue squares, while the best fit is represented by red solid lines. Investigating the line profiles as a function of FWHM of the Mg II and  $H\beta$  (right).

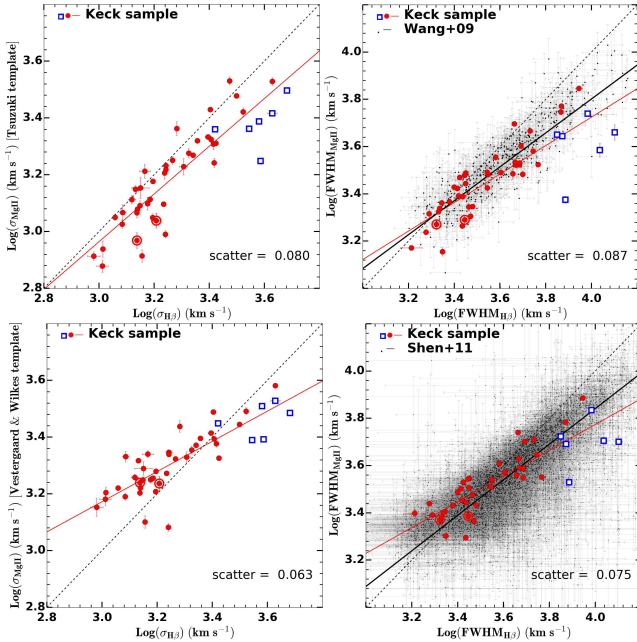


FIG. 6.— Comparison of the line widths of  $H\beta$  and Mg II measured based on Tsuzuki Fe II template (top panels) and Vestergaard & Wilkes template (bottom panels). For FWHMs, Keck sample (red) is plotted along with SDSS AGNs (grey), respectively from Wang et al. (2009) (top) and Shen et al. (2011) (bottom). Note that AGNs with heavy extinction, namely, S16, SS15, S21, W09, and W10 were excluded in our line regression. The solid red line represents the best-fit slope. The six AGNs with very different line profiles between  $H\beta$  and Mg II are shown with open blue squares. The AGNs with a hint of internal extinction in the Mg II region (SS5 and SS12) are marked with larger red open circles. The rms scatter of the best fit is shown as text in the plot.

which is represented by the Big Blue Bump (BBB), for more luminous AGNs (Malkan & Sargent 1982; Zheng & Malkan 1993). Thus, for given photoionizing flux and the emission line luminosity, the continuum luminosity close to BBB will be higher for more luminous AGNs. The sub-linear relation between Mg II and UV continuum luminosity is also reported to be related with physical parameters, i.e., Eddington ratio (see, for example, Dong et al. 2009). The linear relation between  $H\beta$  and optical continuum luminosity at 5100Å indicates that the effect of the increasing thermal component is

relatively weak at 5100Å, which is well off the BBB.

Last, we also compare  $L_{\text{MgII}}$  with  $L_{H\beta}$  and obtained the best-fit slope  $0.66 \pm 0.11$  ( $\sigma_{\text{int}} = 0.20 \pm 0.02$ ) for the Keck sample. For the combined sample of Keck and SDSS AGNs from Wang et al. (2009), we obtained the best-fit slope of  $0.83 \pm 0.02$  ( $\sigma_{\text{int}} = 0.15 \pm 0.01$ ), which is close to the slope of  $L_{\text{MgII}}$  vs.  $L_{5100}$ .

In summary, we obtained an almost linear relation between  $L_{5100}$  and  $L_{3000}$  while the relation is sub-linear between  $L_{5100}$  and  $L_{\text{MgII}}$ . Also, we find that the slope between UV and optical luminosities varies depending on the sample. For  $M_{\text{BH}}$  calibrations, we will use the correlation results expressed with Equation 4, 5, 6 in the next section. However, since the correlation slope depends on the sample and the dynamic range, we will also calibrate UV mass estimators without using these correlations.

### 4.3. Calibrating $M_{\text{BH}}$ estimators

To calibrate  $M_{\text{BH}}$  estimators we determine the coefficients in Eq. 1 for each pair of velocity and luminosity measurements based on  $H\beta$ , Mg II, UV and optical continuum, by comparing the UV-based mass with the reference  $M_{\text{BH}}$ . As the reference mass, we adopt the  $M_{\text{BH}}$  estimated based on  $H\beta$  line dispersion and  $L_{5100}$ , by combining the virial theorem (i.e.,  $\beta=2$ ) and the  $H\beta$  size-luminosity relation from Bentz et al. (2013) (i.e.,  $\gamma=0.533$ ). For  $\alpha$ , we adopt the virial factor  $f=4.47$  from Woo et al. (2015) based on the calibration of AGN  $M_{\text{BH}}$ -stellar velocity dispersion relation, which corresponds to  $\alpha=7.47$  (see Appendix in Woo et al. 2015).

#### 4.3.1. $H\beta$ -based mass estimators

In Figure 8, we first calibrate optical mass estimators based on  $H\beta$ . For  $H\beta$  line dispersion, we fixed  $\beta$  as 2 (top panels), while for  $H\beta$  FWHM we used  $\beta=2/1.16=1.72$  since  $\log \text{FWHM}_{H\beta} \propto 1.16 \log \sigma_{H\beta}$  (see Figure 5). Also, when we used  $L_{H\beta}$ , we adopted the correlation result between  $L_{H\beta}$  and  $L_{5100}$  from Eq. 4, which corresponds to  $\gamma=0.533/0.99=0.54$ . The rms scatter between two mass estimates is  $\sim 0.1$ - $0.14$  dex, indicating that the choice of velocity measure (either FWHM or line dispersion) or the choice of luminosity (i.e., either continuum luminosity at 5100Å or line luminosity of  $H\beta$ ) adds small additional systematic uncertainties. However, this assessment only applies when the data quality, hence the mea-

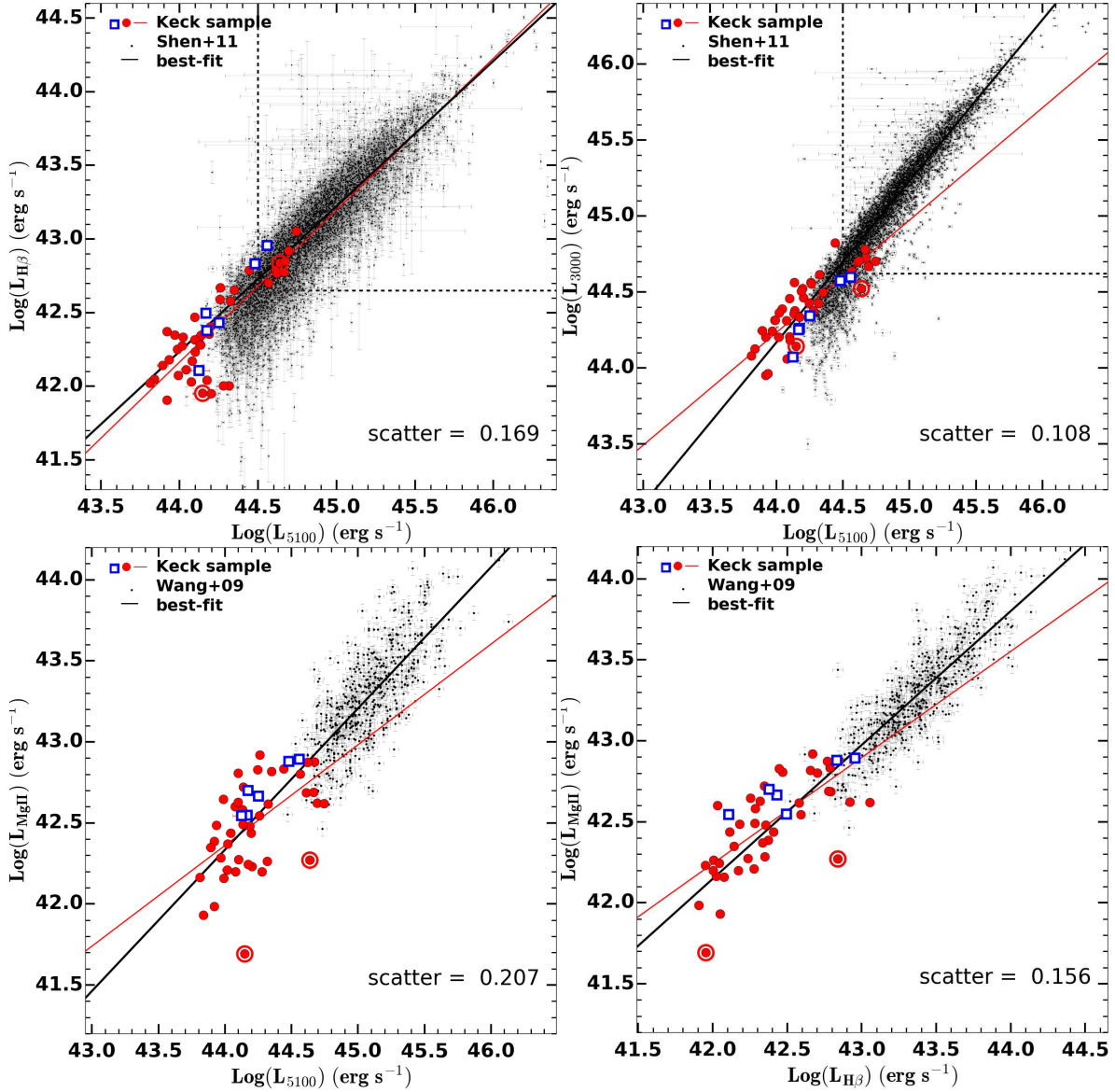


FIG. 7.— Comparison of various luminosities. Top panels show  $L_{5100}$  vs.  $L_{H\beta}$  (left) and  $L_{5100}$  vs.  $L_{3000}$  (right) with the Keck (red circles) and SDSS AGNs from Shen et al. (2011) (grey points). Bottom panels present  $L_{5100}$  vs.  $L_{MgII}$  (left) and  $L_{H\beta}$  vs.  $L_{MgII}$  (right) with the Keck AGNs (red) and SDSS AGNs from Wang et al. (2009) (grey cross). Red and black solid lines represent the best-fit for the Keck sample, and the combined sample of Keck and SDSS AGNs, respectively. The six AGNs with very different line profiles between Mg II and H $\beta$  (blue squares) do not significantly affect the best-fit results. Two AGNs, SS5 and SS12 with a hint of internal extinction in the Mg II region are marked with larger red open circles.

surement uncertainty is comparable to those of our Keck sample. In comparing our result based on the enlarged sample over a large dynamic range with our previous result based on the limited subsample (see Table 3 in McGill et al. 2008), we find that our new calibration is more reliable since the scatter is significantly reduced by 0.1–0.19 dex.

#### 4.3.2. Mg II-based mass estimators

We calibrate UV mass estimators by comparing  $M_{BH}$  estimated based on Mg II line with the reference  $M_{BH}$  based on H $\beta$ . First, we adopt the  $\beta$  value from the direct comparison of H $\beta$  line dispersion with Mg II line dispersion as well as Mg II FWHM, respectively. In other words, for Mg II line dispersion,  $\beta = 2/0.84 = 2.38$  since  $\log \sigma_{MgII} \propto 0.84 \log \sigma_{H\beta}$ , while  $\beta = 2/0.70 = 2.85$  for Mg II FWHM since  $\log FWHM_{MgII} \propto 0.70 \log \sigma_{H\beta}$  (see § 4.1). For luminosity, we also use the results from Section 4.2. Since  $L_{3000} \propto 1.06 L_{5100}$ , we adopted

$\gamma = 0.53/1.06 = 0.50$  for  $L_{3000}$ . In the case of  $L_{MgII}$ , we used  $\gamma = 0.53/0.87 = 0.61$  since  $L_{MgII} \propto 0.87 L_{5100}$ . Using these fixed  $\beta$  and  $\gamma$  values, we performed the  $\chi^2$  minimization with the FITEXY method (Park et al. 2012b) to determine  $\alpha$  (see Figure 9). In general the scatter is larger than 0.2 dex and the consistency with H $\beta$ -based mass is better for Mg II line dispersion than FWHM. Also, continuum luminosity at 3000 Å provides a better calibration than the line luminosity of Mg II.

Since the six AGNs with strong discrepancy of line profiles between H $\beta$  and Mg II are more scattered from the best-fit relation as explained (open blue squares in Figure 9), we investigate how the calibration improves if we exclude these 6 AGNs. By removing the six AGNs, we obtained slightly better calibration with smaller scatter as presented in Table 3. Note that after removing these 6 AGNs, the  $\beta$  becomes close to 2 as expected from a virial relation.



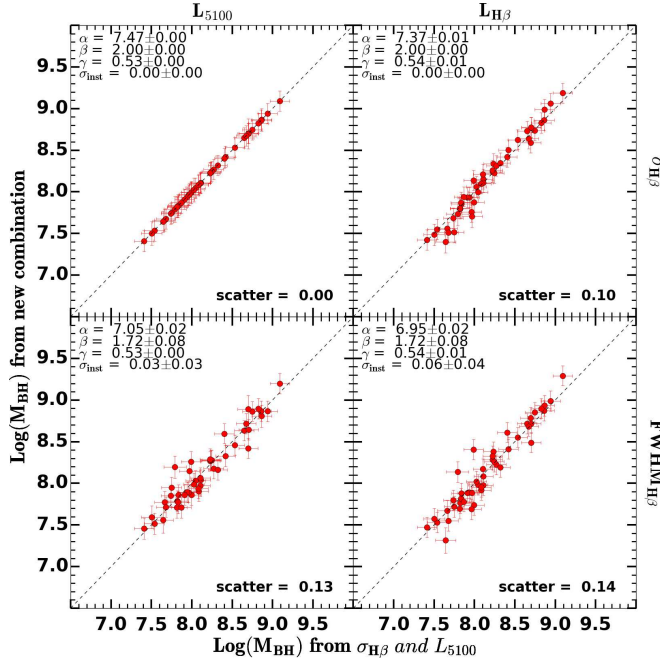


FIG. 8. — Cross-calibration fitting between newly derived  $M_{\text{BH}}$  and fiducial mass with estimators from  $\text{H}\beta$  line. X axis data points represent our target’s fiducial mass, while y axis data points are  $M_{\text{BH}}$  from  $\alpha + \beta \log V_{1000} + \gamma \log L$ .  $V_{1000}$  means velocity estimator using  $1000 \text{ km s}^{-1}$  unit,  $L$  is luminosity estimator having  $10^{44} \text{ erg s}^{-1}$  unit for continuum or  $10^{42} \text{ erg s}^{-1}$  unit for emission line.  $\beta$  and  $\gamma$  in each panel depend on a kind of estimators which are shown in upper left part of figure, and  $\alpha$  is estimated by  $\chi^2$  minimization fitting.

Second, instead of using the correlation analysis between UV and optical luminosities and line widths, we simply fix  $\beta=2$  and  $\gamma=0.5$ , following a virial relation and the expected size-luminosity relation, regardless of the choice of velocity measure (either Mg II line dispersion or FWHM) and luminosity measure (either  $L_{3000}$  or  $L_{\text{MgII}}$ ) (middle panels in Figure 9). In this case, we obtained somewhat smaller scatter. For fixed  $\beta$  and  $\gamma$ , the result does not change significantly with/without removing the six AGNs with very different line profiles between  $\text{H}\beta$  and Mg II.

Third, we also tried to calibrate the UV mass estimators by fixing  $\beta=2$  or by fixing  $\gamma=0.5$ , respectively. For these cases, the scatter is similar to the case with fixed  $\beta$  and  $\gamma$  while the coefficient  $\alpha$  varies by 0.1-0.2 dex. Finally, we let all coefficients,  $\alpha$ ,  $\beta$ , and  $\gamma$  freely vary, and obtain the best-fit results (right panel in Figure 9). Again, we do not find a significant improvement in scatter.

Based on these results we find that the pair of Mg II line dispersion and  $L_{3000}$  provides the best calibration with a  $\sim 0.2$  dex scatter than any other pair of velocity and luminosity measures. Among the various choice of  $\beta$  and  $\gamma$ , we find no significant difference or improvement, indicating that a simple approach assuming the virial relation (i.e.,  $\beta=2$ ) and the expected size-luminosity relation (i.e.,  $\gamma=0.5$ ) is comparable to the calibration based on UV-optical comparisons of luminosities, and velocities, respectively, or to the calibration using the  $\alpha$ ,  $\beta$ , and  $\gamma$  coefficients as free parameters.

Compared to our previous results based on a subsample of the current data (McGill et al. 2008), we obtained improved calibrations with smaller intrinsic scatters. The intrinsic scatter between  $\text{H}\beta$ -based and Mg II-based masses is around 0.17-0.28 dex while the rms scatter is around 0.2-0.3 dex. For the best calibration (i.e., based on Mg II line disper-

sion and  $L_{3000}$ ), the intrinsic scatter between  $\text{H}\beta$ -based mass and Mg II-based mass is  $\sim 0.17$  dex, indicating that even with the measurements based on high quality spectra, the single-epoch mass determined from UV measurements suffers from additional uncertainties by more than 0.17 dex, if we assume the  $\text{H}\beta$ -based mass represents the true  $M_{\text{BH}}$ .

As a consistency check, we also performed the same calibration for Mg II-based masses, using the fiducial mass determined from FWHM of  $\text{H}\beta$  and  $L_{5100}$  (for the issues on the FWHM vs.  $\sigma$ , see Peterson et al. 2004; Collin et al. 2006; Denney et al. 2009; Park et al. 2012a). As presented in Table 4, we obtained slightly worse calibrations with a larger scatter. Again, the line dispersion of Mg II ( $\sigma_{\text{MgII}}$ ) and  $L_{3000}$  provides the best calibration among all pairs of velocity and luminosity measures.

## 5. DISCUSSION

### 5.1. Systematic uncertainties in Mg II-based mass estimates

Although the single-epoch estimators are powerful in determining  $M_{\text{BH}}$  of a large sample, the uncertainty of the mass estimates is much more significant than that of the reverberation masses, due to the uncertainty and scatter of the size-luminosity relation (e.g., 0.19 dex reported by Bentz et al. 2013). Moreover, there are additional sources of uncertainties in Mg II-based mass estimates since these mass estimates are based on further calibrations of the Mg II line velocity and UV luminosities against  $\text{H}\beta$ -based  $M_{\text{BH}}$  since there is no available Mg II-based size-luminosity relation.

Here, we discuss several issues to consider in understanding the systematic uncertainties of Mg II-based mass estimates. First, while the variability is the key to measure the BLR size, it also causes a difficulty in calibrating mass estimators. Since for given AGNs with a fixed  $M_{\text{BH}}$ , luminosity and velocity varies over time, simultaneous observations of the rest-frame UV and optical are required to properly compare the widths of  $\text{H}\beta$  and Mg II or the UV and optical luminosities. The non-simultaneity often causes difficulties in comparing C IV and  $\text{H}\beta$  line widths (see Denney 2012), while it can be avoided by selecting AGNs at optimal redshifts so that both Mg II and  $\text{H}\beta$  lines can be simultaneously obtained in the observed spectral range (e.g., McGill et al. 2008; Wang et al. 2009; Shen et al. 2011).

Instead of the continuum luminosity at  $3000\text{\AA}$ , the line luminosity of Mg II can be utilized to determine  $M_{\text{BH}}$  by assuming that Mg II line luminosity varies in response to UV continuum luminosity (for example, see a recent study by Zhu et al. 2017). As we have shown in Figure 7, the scatter increases by a factor of 2 when we compare  $L_{5100}$  with  $L_{\text{MgII}}$  instead of  $L_{3000}$ . Due to this less tight correlation, the uncertainty of  $M_{\text{BH}}$  estimates based on  $L_{\text{MgII}}$  will be larger than those based on  $L_{3000}$  (see the scatter in Figure 9).

Second, Balmer continuum present in the UV spectral range may cause a systematic uncertainty in measuring UV continuum luminosity. Without a proper fitting and subtraction of Balmer continuum,  $L_{3000}$  may be overestimated, resulting in a higher  $M_{\text{BH}}$ . However, the systematic effect of Balmer continuum is limited since the contribution of Balmer continuum at  $3000\text{\AA}$  is relatively small. For example, Kovačević-Dojčinović et al. (2017) reported that  $L_{3000}$  changes by  $\sim 10\%$  on average, hence,  $M_{\text{BH}}$  is overestimated by an average  $\sim 5\%$ .

Third, various studies reported a non-linear relationship between  $\text{H}\beta$  and Mg II line widths (Salviander et al. 2007; Wang et al. 2009; Shen et al. 2011). The FWHM of  $\text{H}\beta$  is larger than

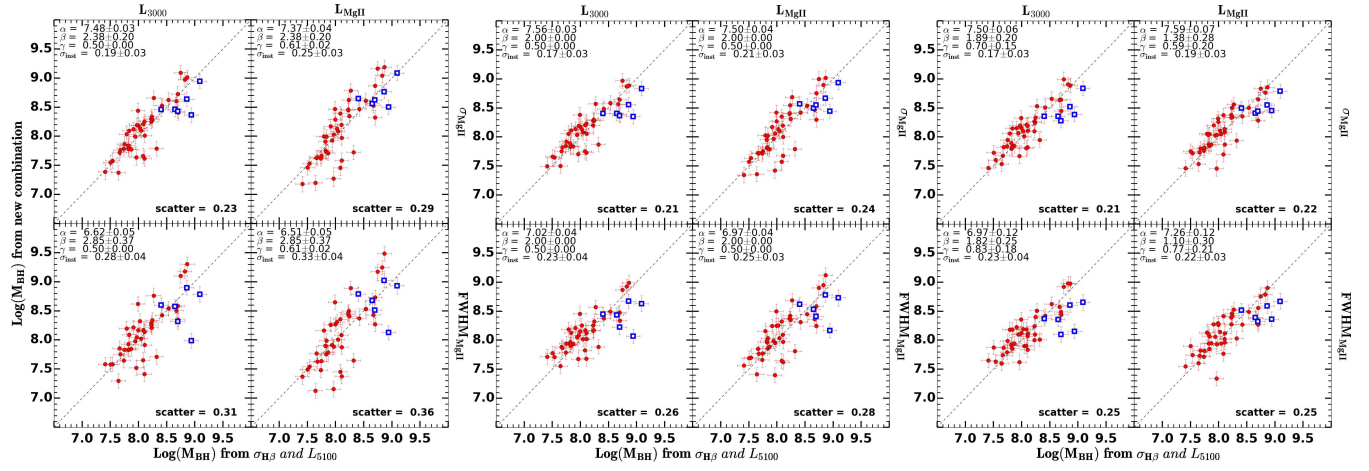


FIG. 9.— Similar as Figure 8 but with estimators from Mg II line. Left panels:  $\beta$  and  $\gamma$  are obtained from the results of line width and luminosity comparison in Section 4.1 and 4.2. Middle panels: We fixed  $\beta=2$  and  $\gamma=0.5$ , following a virial relation and the expected size-luminosity relation. Right panels:  $\beta$  and  $\gamma$  are from the best-fit results. Open blue squares show the six AGNs with very different line profiles between H $\beta$  and Mg II.

TABLE 3  
M<sub>BH</sub> ESTIMATORS BASED ON MG II, USING THE FIDUCIAL MASS FROM  $\sigma_{H\beta}$  AND  $L_{51000}$

Case (1)	N (2)	$\alpha$ (3)	$\beta$ (4)	$\gamma$ (5)	$\sigma_{int}$ (6)	rms (7)	$\alpha$ (8)	$\beta$ (9)	$\gamma$ (10)	$\sigma_{int}$ (11)	rms (12)
<b>L<sub>3000</sub> &amp; <math>\sigma_{MgII}</math></b>							<b>L<sub>3000</sub> &amp; FWHM<sub>MgII</sub></b>				
1) $\beta$ & $\gamma$ from scaling	47	7.48 $\pm$ 0.03	2.38 $\pm$ 0.20	0.50 $\pm$ 0.00	0.19 $\pm$ 0.03	0.23	6.62 $\pm$ 0.05	2.85 $\pm$ 0.37	0.50 $\pm$ 0.00	0.28 $\pm$ 0.04	0.31
	41	7.52 $\pm$ 0.03	1.98 $\pm$ 0.12	0.50 $\pm$ 0.00	0.13 $\pm$ 0.04	0.18	6.83 $\pm$ 0.03	2.32 $\pm$ 0.23	0.50 $\pm$ 0.00	0.20 $\pm$ 0.03	0.23
2) $\beta=2$ & $\gamma=0.5$	47	<b>7.56 <math>\pm</math> 0.03</b>	<b>2.00</b>	<b>0.50</b>	<b>0.17 <math>\pm</math> 0.03</b>	<b>0.21</b>	<b>7.02 <math>\pm</math> 0.04</b>	<b>2.00</b>	<b>0.50</b>	<b>0.23 <math>\pm</math> 0.04</b>	<b>0.26</b>
3) $\beta = 2$	47	7.48 $\pm$ 0.06	2.00	0.69 $\pm$ 0.14	0.17 $\pm$ 0.03	0.21	6.89 $\pm$ 0.07	2.00	0.83 $\pm$ 0.18	0.22 $\pm$ 0.04	0.25
4) $\gamma=0.5$	47	7.57 $\pm$ 0.05	1.92 $\pm$ 0.19	0.50	0.17 $\pm$ 0.03	0.21	7.10 $\pm$ 0.13	1.83 $\pm$ 0.25	0.50	0.23 $\pm$ 0.04	0.26
Free $\beta$ & $\gamma$	47	7.50 $\pm$ 0.06	1.89 $\pm$ 0.20	0.70 $\pm$ 0.15	0.17 $\pm$ 0.03	0.21	6.97 $\pm$ 0.12	1.82 $\pm$ 0.25	0.83 $\pm$ 0.18	0.23 $\pm$ 0.04	0.25
<b>L<sub>MgII</sub> &amp; <math>\sigma_{MgII}</math></b>							<b>L<sub>MgII</sub> &amp; FWHM<sub>MgII</sub></b>				
1) $\beta$ & $\gamma$ from scaling	47	7.37 $\pm$ 0.04	2.38 $\pm$ 0.20	0.61 $\pm$ 0.02	0.25 $\pm$ 0.03	0.29	6.51 $\pm$ 0.05	2.85 $\pm$ 0.37	0.61 $\pm$ 0.02	0.33 $\pm$ 0.04	0.36
	41	7.43 $\pm$ 0.04	1.98 $\pm$ 0.12	0.61 $\pm$ 0.02	0.21 $\pm$ 0.04	0.25	6.74 $\pm$ 0.04	2.32 $\pm$ 0.23	0.61 $\pm$ 0.02	0.26 $\pm$ 0.04	0.29
2) $\beta=2$ & $\gamma=0.5$	47	<b>7.50 <math>\pm</math> 0.04</b>	<b>2.00</b>	<b>0.50</b>	<b>0.21 <math>\pm</math> 0.03</b>	<b>0.24</b>	<b>6.97 <math>\pm</math> 0.04</b>	<b>2.00</b>	<b>0.50</b>	<b>0.25 <math>\pm</math> 0.03</b>	<b>0.28</b>
3) $\beta = 2$	47	7.57 $\pm$ 0.07	2.00	0.36 $\pm$ 0.13	0.21 $\pm$ 0.03	0.24	6.97 $\pm$ 0.09	2.00	0.50 $\pm$ 0.17	0.25 $\pm$ 0.03	0.28
4) $\gamma=0.5$	47	7.61 $\pm$ 0.05	1.48 $\pm$ 0.19	0.50	0.19 $\pm$ 0.03	0.22	7.27 $\pm$ 0.13	1.37 $\pm$ 0.24	0.50	0.23 $\pm$ 0.03	0.26
5) Free $\beta$ & $\gamma$	47	7.59 $\pm$ 0.07	1.38 $\pm$ 0.28	0.59 $\pm$ 0.20	0.19 $\pm$ 0.03	0.22	7.26 $\pm$ 0.12	1.10 $\pm$ 0.30	0.77 $\pm$ 0.21	0.22 $\pm$ 0.03	0.25

NOTE. — Col. (1): Method of calibration. Col. (2): Number of data use in the calibration. Col. (3) & (8):  $\alpha$  values. Col. (4) & (9):  $\beta$  values. Col. (5) & (10):  $\gamma$  values. Col. (6) & (11): intrinsic scatter. Col. (7) & (12): rms scatter.

TABLE 4  
M<sub>BH</sub> ESTIMATORS BASED ON MG II, USING THE FIDUCIAL MASS FROM  $FWHM_{H\beta}$  AND  $L_{51000}$

Case (1)	N (2)	$\alpha$ (3)	$\beta$ (4)	$\gamma$ (5)	$\sigma_{int}$ (6)	rms (7)	$\alpha$ (8)	$\beta$ (9)	$\gamma$ (10)	$\sigma_{int}$ (11)	rms (12)
<b>L<sub>3000</sub> &amp; <math>\sigma_{MgII}</math></b>							<b>L<sub>3000</sub> &amp; FWHM<sub>MgII</sub></b>				
1) $\beta$ & $\gamma$ from scaling	47	7.36 $\pm$ 0.04	2.89 $\pm$ 0.16	0.50 $\pm$ 0.00	0.21 $\pm$ 0.03	0.25	6.38 $\pm$ 0.05	3.33 $\pm$ 0.27	0.50 $\pm$ 0.00	0.30 $\pm$ 0.05	0.33
	41	7.31 $\pm$ 0.04	2.89 $\pm$ 0.16	0.50 $\pm$ 0.00	0.19 $\pm$ 0.03	0.23	6.33 $\pm$ 0.04	3.33 $\pm$ 0.27	0.50 $\pm$ 0.00	0.25 $\pm$ 0.04	0.28
2) $\beta=2$ & $\gamma=0.5$	47	7.54 $\pm$ 0.03	2.00	0.50	0.21 $\pm$ 0.03	0.24	7.01 $\pm$ 0.04	2.00	0.50	0.26 $\pm$ 0.04	0.29
3) $\beta = 2$	47	7.50 $\pm$ 0.08	2.00	0.61 $\pm$ 0.16	0.21 $\pm$ 0.03	0.24	6.91 $\pm$ 0.09	2.00	0.74 $\pm$ 0.20	0.26 $\pm$ 0.04	0.29
4) $\gamma=0.5$	47	7.47 $\pm$ 0.04	2.38 $\pm$ 0.21	0.50	0.20 $\pm$ 0.03	0.23	6.84 $\pm$ 0.13	2.35 $\pm$ 0.27	0.50	0.26 $\pm$ 0.04	0.29
5) Free $\beta$ & $\gamma$	47	7.44 $\pm$ 0.06	2.36 $\pm$ 0.21	0.58 $\pm$ 0.17	0.20 $\pm$ 0.03	0.23	6.75 $\pm$ 0.12	2.35 $\pm$ 0.25	0.74 $\pm$ 0.21	0.26 $\pm$ 0.05	0.28
<b>L<sub>MgII</sub> &amp; <math>\sigma_{MgII}</math></b>							<b>L<sub>MgII</sub> &amp; FWHM<sub>MgII</sub></b>				
1) $\beta$ & $\gamma$ from scaling	47	7.25 $\pm$ 0.05	2.89 $\pm$ 0.16	0.61 $\pm$ 0.02	0.28 $\pm$ 0.03	0.31	6.27 $\pm$ 0.06	3.33 $\pm$ 0.27	0.61 $\pm$ 0.02	0.35 $\pm$ 0.04	0.38
2) $\beta=2$ & $\gamma=0.5$	47	7.49 $\pm$ 0.04	2.00	0.50	0.21 $\pm$ 0.03	0.25	6.96 $\pm$ 0.04	2.00	0.50	0.26 $\pm$ 0.03	0.29
3) $\beta = 2$	47	7.53 $\pm$ 0.06	2.00	0.42 $\pm$ 0.13	0.22 $\pm$ 0.03	0.25	6.93 $\pm$ 0.08	2.00	0.57 $\pm$ 0.17	0.26 $\pm$ 0.03	0.29
4) $\gamma=0.5$	47	7.51 $\pm$ 0.05	1.93 $\pm$ 0.21	0.50	0.22 $\pm$ 0.03	0.25	7.01 $\pm$ 0.12	1.89 $\pm$ 0.25	0.50	0.26 $\pm$ 0.03	0.29
5) Free $\beta$ & $\gamma$	47	7.53 $\pm$ 0.06	2.02 $\pm$ 0.29	0.42 $\pm$ 0.19	0.22 $\pm$ 0.03	0.25	7.01 $\pm$ 0.12	1.75 $\pm$ 0.34	0.64 $\pm$ 0.23	0.26 $\pm$ 0.03	0.28

NOTE. — Col. (1): Method of calibration. Col. (2): Number of data use in the calibration. Col. (3) & (8):  $\alpha$  values. Col. (4) & (9):  $\beta$  values. Col. (5) & (10):  $\gamma$  values. Col. (6) & (11): intrinsic scatter. Col. (7) & (12): rms scatter.

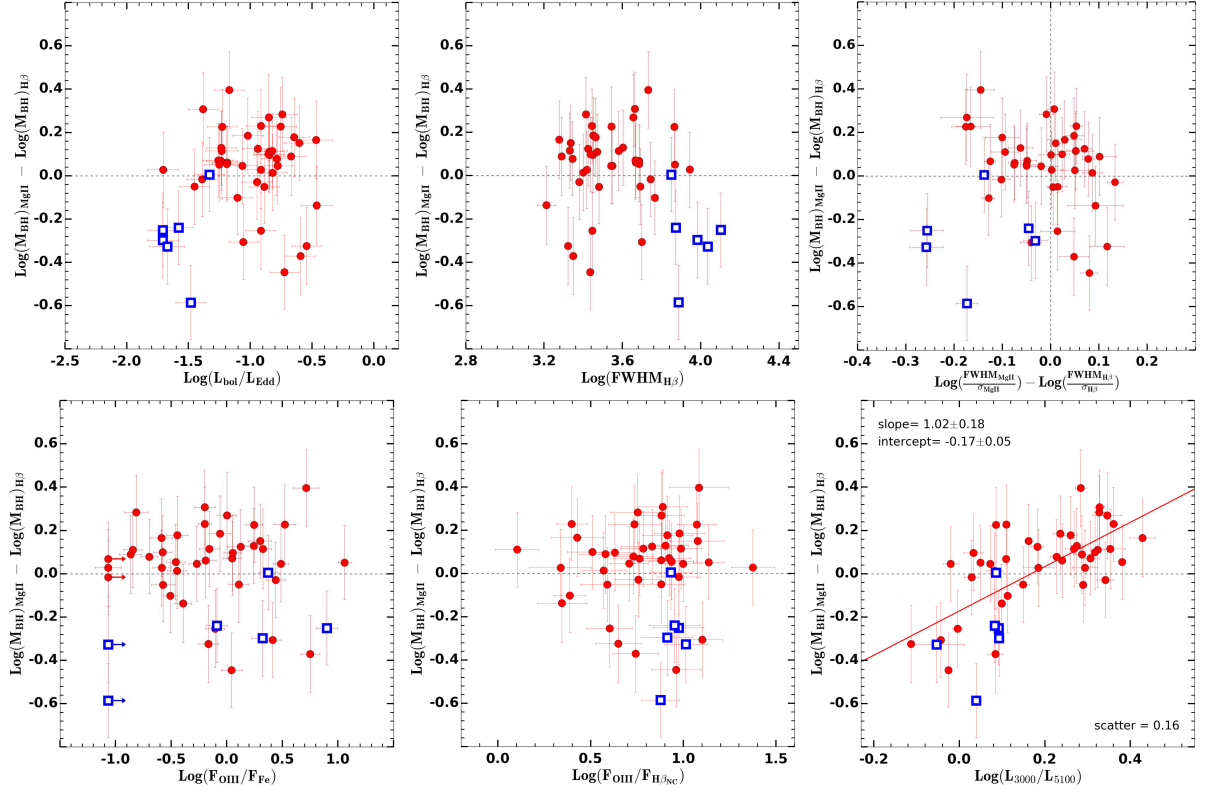


FIG. 10.— Testing systematic trends with Eddington ratio (top left),  $H\beta$  FWHM (top middle), the difference of line profiles between  $H\beta$  and  $Mg\ II$  (top right),  $F_{OIII}/F_{FeII}$  (bottom left),  $F_{OIII}/F_{H\beta, narrow}$  (bottom middle),  $L_{3000}/L_{5100}$  (bottom right). Open blue squares show the six AGNs, S23, S24, W02, W03, W12, W20, with very different line profiles between  $Mg\ II$  and  $H\beta$ .



that of Mg II by more than 20% for AGNs with a very broad H $\beta$  line (Marziani et al. 2013) while the line widths of H $\beta$  and Mg II are more consistent in AGNs with a narrower H $\beta$  line. This non-linear relationship may cast doubts on Mg II-based mass estimates since while  $\beta=2$  is used for H $\beta$  line in Eq. 1,  $\beta$  is forced to be larger than 2 for Mg II, violating the virial assumption. It is not clear whether H $\beta$  line width overestimates the true velocity of BLR gas when the FWHM of H $\beta$  is larger than, for example, 4000 km s $^{-1}$  (see the discussion on Population B in Marziani et al. 2013), or Mg II line width underestimates the velocity of BLR gas. The fact that the line profile of Mg II is rather similar to each other, regardless of the width of the line (see Figure 4) may imply that there is a systematic issue in measuring the H $\beta$  line width, particularly, FWHM, when the line is extremely broad. In practice, we performed the calibration with/without using the correlation results between H $\beta$  and Mg II line widths. It seems better to assume a virial relation (i.e.,  $\beta=2$ ) since the Mg II-H $\beta$  width correlation results depend on the sample and dynamic range, suffering from systematic effects.

Fourth, it is not clear whether the narrow component of Mg II should be separately fitted and subtracted to properly measure the width of the broad component of Mg II. Subtracting the narrow component originated from the narrow-line region is a typical process in fitting and measuring the width of the broad component of H $\beta$ , by assuming the narrow H $\beta$  profile is identical to other narrow lines, i.e., O III  $\lambda$ 5007. In the case of Mg II, however, it is practically difficult to constrain the profile of the narrow component. Thus, most previous studies do not attempt to subtract the narrow component. In contrast, Wang et al. (2009) used two components, respectively for the broad and narrow components in Mg II, and measured the FWHM of the broad component to determine  $M_{\text{BH}}$ . However, FWHM measurements suffer from significant uncertainties since the peak of the line profile will be strongly dependent of the amount of flux assigned to the narrow component.

In our study, we see no clear sign of the presence of a narrow component in Mg II even when we see a strong and clear narrow component in H $\beta$ . Note that this can be partly due to the lower spectral resolution in the Mg II area (i.e.,  $\sim 145$  km s $^{-1}$ ), although a narrow line with a typical velocity dispersion of a few hundred km s $^{-1}$  (i.e., in the case of the O III; Woo et al. 2016) can be resolved in our Keck spectra. To test the potential effect of the narrow component in Mg II, we used the O II line profile to constrain the narrow component of Mg II, assuming the profiles of narrow lines in the NLR (i.e., O II and narrow Mg II) are similar. As Malkan et al. (2017) reported that the typical value of Mg II-to-O II ratio in Seyfert 2 galaxies is  $\sim 0.1$ , we take the O II line profile, after multiplying by 0.1, as a narrow component of Mg II and subtract it from the Mg II line to calculate the line width of the broad component of Mg II. However, we find that this practice makes no difference in the line width measurements since O II is much weaker than Mg II, hence the narrow component of Mg II is negligible in most objects. Thus, we did not subtract the potential narrow component and used the total line profile to measure the FWHM and line dispersion. Note that the measurements of line dispersion are not significantly affected by the subtraction or inclusion of the narrow component.

Fifth, we investigated whether the systematic difference between Mg II- and H $\beta$ -based masses shows any dependency on other AGN parameters, i.e., Eddington ratio, FWHM of H $\beta$ ,

the systematic difference of the line profiles between Mg II and H $\beta$  in Figure 10 (top panels). We also check whether the systematic difference of  $M_{\text{BH}}$  is due to the eigenvector 1 by calculating the flux ratio between O III and Fe II, which is integrated in the spectral range and the spectral slope 4434-4684Å (e.g., see Woo et al. 2015), and the flux ratio between O III and the narrow component of H $\beta$  (bottom panel in Figure 10). For the first five parameters, we find no significant trend, suggesting that Mg II-based masses are not significantly biased due to the Eddington ratio, line width, and the Fe II strength.

In contrast, we expect to see a broad trend between the UV to optical mass ratio and the UV to optical luminosity ratio (i.e.,  $L_{3000}/L_{5100}$ ) since single-epoch  $M_{\text{BH}}$  correlates with continuum luminosity as far as the size-luminosity relation (i.e.,  $M_{\text{BH}} \propto L^{0.5}$ ) is used for determining  $M_{\text{BH}}$ . For given  $L_{5100}$  and H $\beta$ -based mass, for example, if the spectral slope becomes steeper (i.e., higher  $L_{3000}/L_{5100}$  ratio), then  $L_{3000}$ , and consequently, Mg II-based mass will be systematically higher. We see this trend in Figure 10. To correct for this systematic trend, we obtain the best-fit slope  $1.02 \pm 0.18$  and the intercept  $-0.17 \pm 0.05$  (last panel in Figure 10), and add the following color correction term to Eq. 1:

$$\Delta C = -1.02 \times \log(L_{3000}/L_{5100}) + 0.17. \quad (7)$$

Since  $L_{5100}$  will not be available for  $M_{\text{BH}}$  determination for high- $z$  AGNs, we can instead use the spectral slope  $\alpha_\lambda$ , with which we model the local UV/optical AGN continuum as a power law,  $f_\lambda \propto \lambda^{\alpha_\lambda}$ . Using  $L_{3000}/L_{5100} = 3000 f_{3000}/5100 f_{5100} = (3000/5100)^{1+\alpha_\lambda}$ , we derive the correction term as a function of  $\alpha_\lambda$ :

$$\Delta C = 0.24(1 + \alpha_\lambda) + 0.17. \quad (8)$$

Note that the mean  $\alpha_\lambda$  of the Keck sample is  $-1.73 \pm 0.60$  (i.e.,  $\alpha_\nu = -0.27 \pm 0.60$ ), which is slightly bluer than the average spectral slope  $\alpha_\nu = -0.44$  of the SDSS quasars (Vanden Berk et al. 2001). Once applied, this correction term will reduce the systematic uncertainty of Mg II-based masses due to the large range of the spectral slope between the UV and optical wavelength range. However, the correction is relatively small. For example, if the spectral slope changes from  $\alpha_\lambda = -1.5$  to  $\alpha_\lambda = -2$ , the correction on  $M_{\text{BH}}$  is  $\sim 0.1$  dex. Thus, if the spectral slope is difficult to determine due to the low S/N, strong Fe II blends, the limited spectral range, or internal dust extinction, this correction can be ignored.

## 5.2. Comparison of various Mg II-based mass estimators

There have been various calibrations of  $M_{\text{BH}}$  estimators based on Mg II in the literature, and here we investigate how  $M_{\text{BH}}$  changes depending on the choice of the estimators. In Figure 11, we present the calculated  $M_{\text{BH}}$  for given pairs of Mg II line width and  $L_{3000}$  based on several UV mass estimators. From our calibrations, we choose Case 2 as the best calibration, and Case 5 as an extreme calibration. In the case of  $M_{\text{BH}}$  based on Mg II line dispersion, McGill et al. (2008) reported the mass calibrators, and we compare our estimators with theirs in the top panels. Case 2 with the fixed  $\beta$  and  $\gamma$  provides a similar  $M_{\text{BH}}$  compared to McGill et al. (2008), with a systematic offset by 0.2-0.3 dex. The difference of the normalization is mainly due to the change of the width measurements. Since for given objects, Mg II line dispersion becomes smaller due to the Tsuzuki et al. (2006) template, that we used in our analysis, while McGill et al. (2008) used the Fe II template of Vestergaard & Wilkes (2001). Thus,  $\alpha$

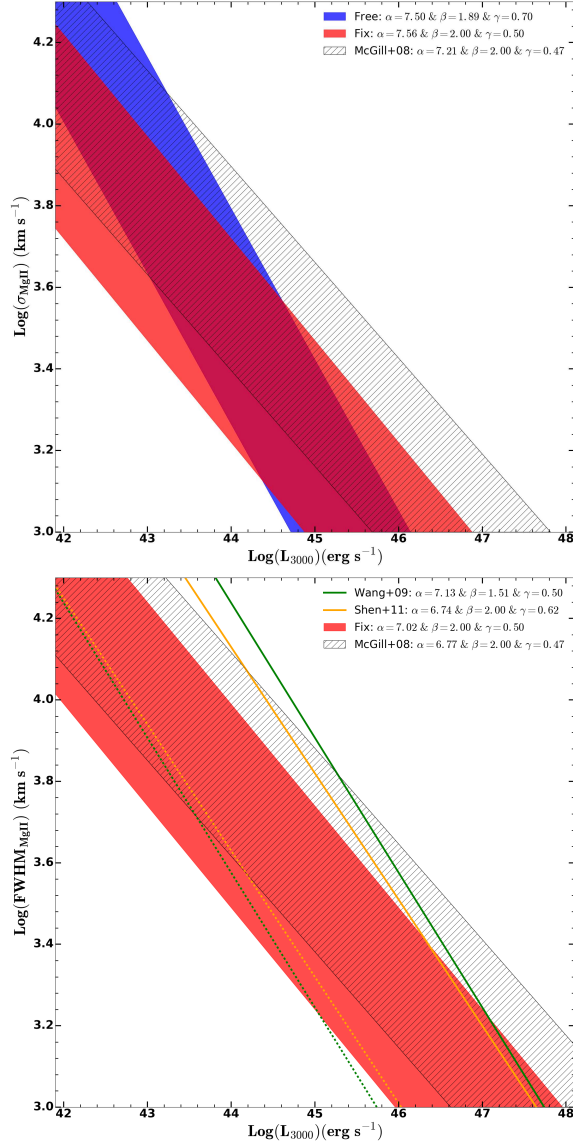


FIG. 11.— Comparison of  $M_{\text{BH}}$  estimates for given pairs of velocity and luminosity measures depending on the choice of UV mass estimator. Top:  $M_{\text{BH}}$  based on Mg II line dispersion from our estimators with fixed  $\beta=2$  &  $\gamma=0.5$  (red area) or free fit results (blue area), compared to that of McGill et al. (2008) (hatched area). For each mass estimator, the area is defined by two equi-mass lines at  $M_{\text{BH}} 10^8$  and  $M_{\text{BH}} 10^9$ , showing the systematic difference among various mass estimators. Bottom:  $M_{\text{BH}}$  based on Mg II FWHM compared to those of Wang et al. (2009) (green line) and Shen et al. (2011) (orange line).

becomes larger for UV-based  $M_{\text{BH}}$  to be consistent with given  $H\beta$ -based mass.

In the case of FWHM, we compare our estimator with those of McGill et al. (2008); Wang et al. (2009); Shen et al. (2011). Compared to Case 2 (red in Figure 11), other estimators derive somewhat lower  $M_{\text{BH}}$ , and the equi-mass line is steeper because of lower  $\beta$  than 2 or higher  $\gamma$  than 0.5. Note that depending on the choice of the estimators,  $M_{\text{BH}}$  will be systematically larger or smaller for AGNs with very broad lines (or lower luminosity). These results indicate that the inferred shape of the mass function of high- $z$  AGNs will be sensitive to the choice of UV  $M_{\text{BH}}$  estimator. Note that for estimating  $M_{\text{BH}}$  using a large survey data, FWHM of Mg II, rather than

line dispersion, is often used since the spectral quality in survey data is not enough to measure the line dispersion of broad lines. Thus, a careful interpretation is required to understand the mass distribution and mass function of high- $z$  AGNs.

## 6. CONCLUSIONS

In this paper, we present a new calibration of  $M_{\text{BH}}$  estimators, using a sample of 52 AGNs at  $z \sim 0.36$  and  $z \sim 0.52$  over the  $M_{\text{BH}}$  range,  $7.4 < \log M_{\text{BH}} < 9$ , for which high quality Keck spectra are available to properly measure line widths and UV and optical luminosities. In addition, we utilize the measurements of SDSS AGNs from literature to increase the dynamic range. The main results are summarized as follows:

(1) There are a number of AGNs, for which  $H\beta$  is much broader than Mg II, particularly for AGNs with a large  $H\beta$  FWHM (see also Wang et al. 2009; Marziani et al. 2013). Consequently, we obtain a sub-linear relationship between Mg II and  $H\beta$  both for FWHM as well as line dispersion.

(2) By comparing optical continuum luminosity at  $5100\text{\AA}$  with UV continuum luminosity and  $H\beta$  line luminosity, we find a correlation close to a linear relationship, while the relation with Mg II line luminosity is somewhat sub-linear, reflecting the Baldwin effect in the UV.

(3) We perform a cross-calibration of  $M_{\text{BH}}$  estimators using various combinations of velocity and luminosity indicators measured from the rest-frame UV and optical spectra, using the mass based on  $H\beta$  line dispersion and  $L_{5100}$  as a reference mass.  $M_{\text{BH}}$  from the new calibrations using  $H\beta$  line and optical luminosities are consistent with each other with an intrinsic scatter less than 0.1 dex and a rms scatter of  $\sim 0.1$  dex.

(4) In the case of UV mass estimators based on Mg II line, the comparison with the reference  $H\beta$ -based masses shows an intrinsic scatter of 0.17-0.28 dex and a rms scatter of  $\sim 0.2$ -0.3 dex, suggesting that there is an additional uncertainty larger than  $\sim 0.2$  dex, depending on a choice of line width (i.e., line dispersion or FWHM) and luminosity measures (i.e.,  $L_{3000}$  or  $L_{\text{MgII}}$ ). Over all, we find that the pair of Mg II line dispersion and  $L_{3000}$  provides the best calibration with an additional  $0.17 \pm 0.03$  dex uncertainty. In the case of  $H\beta$  single-epoch mass estimates, the uncertainties are mainly introduced by three sources. First, the uncertainty of the virial factor, which is 0.12-0.15 dex based on the comparison of the  $M_{\text{BH}}-\sigma_*$  relation between the reverberation-mapped AGNs and quiescent galaxies (Woo et al. 2010, 2015), or 0.4 dex based on the dynamical modeling of the five reverberation-mapped AGNs with velocity-resolved measurements (Pancoast et al. 2014). Second, the scatter in the  $H\beta$  size-luminosity relation is 0.13-0.19 dex, depending on the choice of more reliable measurements (Bentz et al. 2013). Third, the random variability of the line width and luminosity introduces  $\sim 0.1$  dex scatter (Park et al. 2012a). Compared to the total uncertainty of  $H\beta$ -based mass estimates, which can be 0.3-0.4 dex, the additional 0.17-0.28 dex uncertainty from the calibration of UV mass estimators is somewhat smaller. However, the overall uncertainty of Mg II-based mass is larger than that of  $H\beta$  masses.

In this paper, we calibrated UV and optical  $M_{\text{BH}}$  estimators based on single-epoch measurements. While future direct measurements of the Mg II time lag for a sizable sample of AGNs will enable to reduce the systematic uncertainties in the single-epoch mass estimates, the updated and calibrated Mg II mass estimators in this paper will be useful for revisiting  $M_{\text{BH}}$  related issues for high- $z$  AGNs.

This work has been supported by the Basic Science Research Program through the National Research Foundation of Korea government (2016R1A2B3011457 and

No.2017R1A5A1070354). We thank the anonymous referee for useful suggestions.

#### REFERENCES

- Baldwin, J. A. 1977, *ApJ*, 214, 679
- Barth, A. J., Pancoast, A., Thorman, S. J., et al. 2011, *ApJ*, 743, L4
- Barth, A. J., Pancoast, A., Bennert, V. N., et al. 2013, *ApJ*, 769, 128
- Barth, A. J., Bennert, V. N., Canalizo, G., et al. 2015, *ApJS*, 217, 26
- Bennert, V. N., Treu, T., Woo, J.-H., et al. 2010, *ApJ*, 708, 1507
- Bentz, M. C., Peterson, B. M., Pogge, R. W., Vestergaard, M., & Onken, C. A. 2006, *ApJ*, 644, 133
- Bentz, M. C., Peterson, B. M., Netzer, H., Pogge, R. W., & Vestergaard, M. 2009, *ApJ*, 697, 160
- Bentz, M. C., Denney, K. D., Grier, C. J., et al. 2013, *ApJ*, 767, 149
- Blandford, R. D., & McKee, C. F. 1982, *ApJ*, 255, 419
- Boroson, T. A., & Green, R. F. 1992, *ApJS*, 80, 109
- Bruzual, G., & Charlot, S. 2003, *MNRAS*, 344, 1000
- Cackett, E. M., Gültekin, K., Bentz, M. C., et al. 2015, *ApJ*, 810, 86
- Collin, S., Kawaguchi, T., Peterson, B. M., & Vestergaard, M. 2006, *A&A*, 456, 75
- Denney, K. D., Peterson, B. M., Dietrich, M., Vestergaard, M., & Bentz, M. C. 2009, *ApJ*, 692, 246
- Denney, K. D. 2012, *ApJ*, 759, 44
- Dong, X.-B., Wang, T.-G., Wang, J.-G., et al. 2009, *ApJ*, 703, L1
- Fausnaugh, M. M. 2017, *PASP*, 129, 024007
- Ferrarese, L., & Merritt, D. 2000, *ApJ*, 539, L9
- Ferrarese, L., & Ford, H. 2005, *Space Sci. Rev.*, 116, 523
- Gebhardt, K., Bender, R., Bower, G., et al. 2000, *ApJ*, 539, L13
- Greene, J. E., & Ho, L. C. 2005, *ApJ*, 630, 122
- Grier, C. J., Martini, P., Watson, L. C., et al. 2013, *ApJ*, 773, 90
- Karouzos, M., Woo, J.-H., Matsuoka, K., et al. 2015, *ApJ*, 815, 128
- Kaspi, S., Smith, P. S., Netzer, H., et al. 2000, *ApJ*, 533, 631
- Kaspi, S., Maoz, D., Netzer, H., et al. 2005, *ApJ*, 629, 61
- Kormendy, J., & Ho, L. C. 2013, *ARA&A*, 51, 511
- Kovačević-Dojčinović, J., Marčeta-Mandić, S., & Popović, L. Č. 2017, *arXiv:1707.08251*
- Malkan, M. A., Jensen, L. D., Rodriguez, D. R., Spinoglio, L., & Rush, B. 2017, *ApJ*, 846, 102
- Malkan, M. A., & Sargent, W. L. W. 1982, *ApJ*, 254, 22
- Markwardt, C. B. 2009, in *Astronomical Data Analysis Software and Systems XVIII*, ed. D. A. Bohlender, D. Durand, & P. Dowler (San Francisco: ASP), 251
- Marziani, P., Sulentic, J. W., Plauchu-Frayn, I., & del Olmo, A. 2013, *A&A*, 555, A89
- McGill, K. L., Woo, J.-H., Treu, T., & Malkan, M. A. 2008, *ApJ*, 673, 703
- McLure, R. J., & Dunlop, J. S. 2002, *MNRAS*, 331, 795
- McLure, R. J., & Dunlop, J. S. 2004, *MNRAS*, 352, 1390
- McLure, R. J., & Jarvis, M. J. 2002, *MNRAS*, 337, 109
- Metzroth, K. G., Onken, C. A., & Peterson, B. M. 2006, *ApJ*, 647, 901
- Oke, J. B., Cohen, J. G., Carr, M., et al. 1995, *PASP*, 107, 375
- Onken, C. A., Ferrarese, L., Merritt, D., et al. 2004, *ApJ*, 615, 645
- Pancoast, A., Brewer, B. J., Treu, T., et al. 2014, *MNRAS*, 445, 3073
- Park, D., Woo, J.-H., Treu, T., et al. 2012a, *ApJ*, 747, 30
- Park, D., Kelly, B. C., Woo, J.-H., & Treu, T. 2012b, *ApJ*, 203, 6
- Park, D., Woo, J.-H., Bennert, V. et al. 2015, *ApJ*, 799, 164
- Park, S., Woo, J.-H., et al. 2017, *ApJ*, in press
- Peterson, B. M. 1993, *PASP*, 105, 247
- Peterson, B. M., Ferrarese, L., Gilbert, K. M., et al. 2004, *ApJ*, 613, 682
- Reichert, G. A., Rodriguez-Pascual, P. M., Alloin, D., et al. 1994, *ApJ*, 425, 582
- Salviander, S., Shields, G. A., Gebhardt, K., & Bonning, E. W. 2007, *ApJ*, 662, 131
- Schlegel, D. J., Finkbeiner, D. P., & Davis, M. 1998, *ApJ*, 500, 525
- Shen, Y., Richards, G. T., Strauss, M. A., et al. 2011, *ApJS*, 194, 45
- Shen, Y., Horne, K., Grier, C. J., et al. 2016, *ApJ*, 818, 30
- Tremaine, S., Gebhardt, K., Bender, R., et al. 2002, *ApJ*, 574, 740
- Treu, T., Malkan, M. A., & Blandford, R. D. 2004, *ApJ*, 615, L97
- Treu, T., Woo, J.-H., Malkan, M. A., & Blandford, R. D. 2007, *ApJ*, 667, 117
- Tsuzuki, Y., Kawara, K., Yoshii, Y., et al. 2006, *ApJ*, 650, 57
- Vanden Berk, D. E., Richards, G. T., Bauer, A., et al. 2001, *AJ*, 122, 549
- van Dokkum, P. G. 2001, *PASP*, 113, 1420
- Vestergaard, M., & Peterson, B. M. 2006, *ApJ*, 641, 689
- Vestergaard, M., & Wilkes, B. J. 2001, *ApJS*, 134, 1
- Wandel, A., Peterson, B. M., & Malkan, M. A. 1999, *ApJ*, 526, 579
- Vanden Berk, D. E., Richards, G. T., Bauer, A., et al. 2001, *AJ*, 122, 549
- Wang, J.-G., Dong, X.-B., Wang, T.-G., et al. 2009, *ApJ*, 707, 1334
- Woo, J.-H., & Urry, C. M. 2002, *ApJ*, 579, 530
- Woo, J.-H., Treu, T., Malkan, M. A., & Blandford, R. D. 2006, *ApJ*, 645, 900
- Woo, J.-H. 2008, *AJ*, 135, 1849
- Woo, J.-H., Treu, T., Barth, A. J., et al. 2010, *ApJ*, 716, 269
- Woo, J.-H., Schulze, A., Park, D., et al. 2013, *ApJ*, 772, 49
- Woo, J.-H., Yoon, Y., Park, S. et al. 2015, *ApJ*, 801, 38
- Woo, J.-H., Bae, H.-J., Son, D., & Karouzos, M. 2016, *ApJ*, 817, 108
- Zheng, W., & Malkan, M. A. 1993, *ApJ*, 415, 517
- Zhu, D., Sun, M., & Wang, T. 2017, *ApJ*, 843, 30